ACADEMIC PRESS

Available online at www.sciencedirect.com

SCIENCE DIRECT®

Icarus 161 (2003) 319–345

ICARUS

www.elsevier.com/locate/icarus

Forced waves in the martian atmosphere from MGS TES nadir data

D. Banfield,[a,*] B.J. Conrath,[a] M.D. Smith,[b] P.R. Christensen,[c] and R. John Wilson[d]

[a] *Department of Astronomy, Cornell University, Ithaca, NY 14853, USA*
[b] *NASA/Goddard Space Flight Center, Code 690, Greenbelt, MD 20771, USA*
[c] *Department of Geology, Arizona State University, Tempe, AZ 85287, USA*
[d] *NOAA/Geophysical Fluid Dynamics Laboratory, Princeton, NJ 08542, USA*

Received 30 July 2001; revised 17 September 2002

Abstract

We have analyzed the temperature retrievals from Mars Global Surveyor (MGS) Thermal Emission Spectrometer (TES) nadir spectra to yield latitude-height resolved maps of various atmospheric forced wave modes as a function of season for a full Mars year. Among the isolated wave modes is the zonal mean, time mean temperature, which we used to derive zonal mean zonal winds and stationary wave quasi-geostrophic indices of refraction, diagnostic of their propagation. The diurnal Kelvin wave was isolated in the data, with results roughly consistent with models (Wilson and Hamilton, 1996, J. Atmos. Sci. 33, 1290–1326). The $s = 1$ and $s = 2$ stationary waves were found to have significant amplitude in ducts extending up the winter polar jets, while the $s = 3$ stationary wave was found to be confined to near the surface. The $s = 1$ stationary wave was found to have little phase tilt with height during northern winter, but significant westward phase tilt with height in the southern winter. This indicates that the wave carries heat poleward, slightly more than that found in Barnes et al. (1996; J. Geophys. Res. 101, 12,753–12,776). The $s = 1$ stationary wave is likely the dominant mechanism for eddy meridional heat transport for the southern winter. We noted that the phase of the $s = 2$ stationary wave is nearly constant with time, but that the $s = 1$ stationary wave moved 90° of longitude from fall to winter and back in spring in the North. While interannual variability is not yet addressed, overall, these results provide the first comprehensive benchmark for forced waves in Mars's atmosphere against which future atmospheric models of Mars can be compared.

Keywords: Atmospheres; Structure; Mars, atmosphere; Meteorology; Tides, atmospheric

1. Introduction

The behavior of the martian atmosphere can generally be divided into forced and free oscillations. The forced oscillations (the subject of this work) are the atmosphere's response to the daily cycle of the sun, or spatial differences in heating and topography. The free oscillations include atmospheric instabilities, which are generally what one thinks of as "weather" because their behavior is far less regular than the forced modes. On Earth, the forced oscillations, primarily through the stationary waves induced by topography and ocean–continent heating differences, have a strong control over the weather, and thus are important to our everyday lives. Similarly, on Mars, the forced oscillations are important not only through a possible influence on the weather, but also by contributing in a significant way to the overall distribution of heat on the planet. In order to quantitatively map these atmospheric forced oscillations, we have analyzed Mars Global Surveyor (MGS) Thermal Emission Spectrometer (TES) atmospheric temperature retrievals.

The forced oscillations consist of thermal tides and stationary waves. The thermal tides are relatively strong on Mars compared to the Earth. The small mass of the atmosphere and its radiative activity (through both dust and CO_2 absorption) allow it to heat and cool significantly throughout a solar day or sol. The tides have been investigated theoretically in detail by Lindzen (1970), Zurek (1976), Conrath (1976), and subsequent papers; through numerical models by Wilson and Hamilton (1996), Bridger and Mur-

* Corresponding author. Fax: +1-607-255-9002.
E-mail address: banfield@astro.cornell.edu (D. Banfield).

0019-1035/03/$ – see front matter © 2003 Elsevier Science (USA). All rights reserved.
doi:10.1016/S0019-1035(02)00044-1

phy (1998), and others; and observationally from orbit by Pirraglia and Conrath (1974), Martin et al. (1979), Conrath (1981), Banfield et al. (2000), Wilson (2000), Wilson and Richardson (2000), and Wilson (2002). The thermal tides are expected to play a large role in determining the winds at the surface and may be critical in the development of dust storms. The thermal tides consist not only of modes that follow the sun (so-called migrating tides), but also, through their interaction with topography they have modes which do not follow the sun, nonmigrating tides. These nonmigrating tides (including some which happen to be resonantly amplified Kelvin waves in the special case of Mars) are expected to exert their strongest influence in the upper atmosphere, modulating the atmospheric density at ~130 km and hence the aerobraking experienced by orbiters (Forbes and Hagan, 2000; Wilson, 2000, 2002). While the data set analyzed in this work is not ideal for isolating and quantifying the thermal tides, it does represent the most complete global view of a seasonal progression of the tides. The observations do a good job of identifying the diurnal and semidiurnal Kelvin waves throughout the martian year of the lowest several scale heights, which should allow an interesting connection to the higher altitude (aerobraking) observations.

The stationary waves can influence the stability of the atmosphere, enhancing the formation of disturbances at certain longitudes and impeding their formation at others (Hollingsworth et al. (1996). This is their familiar role on the Earth, but on both Earth and Mars they also play a significant role in the redistribution of heat from the equator to the poles (Hollingsworth and Barnes, 1996; Barnes et al., 1996; Nayvelt et al., 1997). Conrath (1981) observed in the Mariner 9 IRIS data what may have been a stationary wave, but the data were not able to discriminate between that and a transient wave. The stationary waves were measured by Banfield et al. (1996), whose results are still valid in spite of the likely contamination of IRTM T15 data by surface radiance (Wilson and Richardson, 2000) which mainly distorted their tidal solutions. Banfield et al. (2000) were able to isolate the $s = 1$ and $s = 2$ stationary waves in the premapping TES data, but their coverage was only for part of the southern hemisphere, and for the part of the year centered on northern winter. Wilson (2000) shows the stationary wave pattern in TES data at $L_s \sim 120°$–$140°$ and states that it is present in the southern hemisphere from $L_s \sim 108°$–$220°$. Most recently, Hinson et al. (2001) identified both stationary waves and thermal tides in radio occultations from MGS for one value of L_s (~75°) and one latitude (~66*N*). The present work represents the most complete observations of the stationary waves to date in both spatial and seasonal coverage.

The difficulty involved in quantifying these various atmospheric modes results from the MGS TES observations being limited to only two local times. Because of this sampling strategy, certain stationary waves and thermal tides are aliased to appear identical to one another. This work focuses not only on quantifying the different modes, but also identifying and separating them to the extent that is possible. In addition to our particular analysis techniques, we have also used the GFDL Mars Global Circulation Model (MGCM) (e.g., Wilson and Hamilton, 1996; Wilson and Richardson, 2000) to help identify which modes are dominant. We also use the MGCM to help interpret the tidal observations.

We will discuss the nature and limitations of the TES data set and its atmospheric retrievals upon which this analysis is based. Then we will go on to discuss the technique we have used to maximize our ability to discriminate between different types of atmospheric forced oscillations given our observational sequences. We will first present the zonal mean temperature, and use it to derive zonal mean zonal winds and the quasi-geostrophic indices of refraction for the gravest three stationary waves. Then we will discuss the different modes isolated in turn. We will also compute the meridional heat transports for the modes and end with a summary.

2. Data set

This study focuses on retrieved temperatures from the infrared spectra taken by the TES instrument on the MGS spacecraft. Specifically, the data we have analyzed in this work were taken when Mars Global Surveyor was in its mapping orbit, a sun-synchronous, high-inclination orbit, from March 1999 to January 2001, i.e., almost exactly 1 Mars year. This is distinct from the aerobraking and science phasing data that were analyzed in Banfield et al. (2000), which were biased toward the southern hemisphere and had limited seasonal coverage, much less regular spatial sampling, but better local time sampling. The short period and high inclination of MGS' mapping orbit allowed near-global coverage over short time scales (less than or of order 1 day for low zonal wavenumbers). The regular, sun-synchronous phasing of the mapping orbit makes certain facets of the data analysis cleaner (e.g., avoiding the need to bin extensively in local time), while at the same time introducing its own set of peculiarities (which we will discuss more later).

2.1. Coverage

The TES instrument can be used to take spectra of the planet from any emission angle, including "limb scans" where the atmosphere above the limb is viewed at a range of tangent heights. However, the majority of TES data, and the data used in this study were all taken within 10° of nadir, with a typical emission angle being about 0.5°. This reduces the vertical resolution and maximum height ultimately realizable in the retrieved temperature profiles compared to limb scans, but minimizes the horizontal extent of the area sampled in each observation. It also makes for a relatively

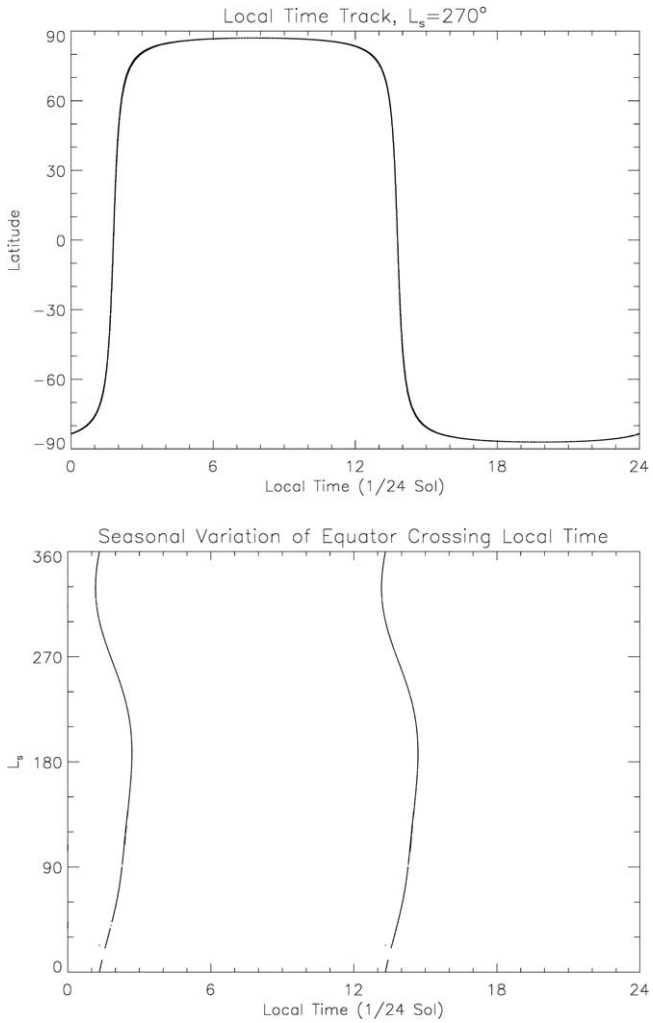

Fig. 1. Local time dependencies of observations. (a) Shows the latitudinal dependence of the local time of the observations for $L_s = 270°$. (b) Shows the seasonal dependence of the local time of the equatorial observations.

uniform data set, with the geometry changing minimally from one observation to another, and thus minimizing errors induced due to systematic geometric effects.

With the TES data processing in use for this analysis, observations exist with latitudinal resolution up to 0.1°. However, primarily due to downlink data rate limitations, the coverage is not always complete at this resolution. Instead, several orbits worth of data are typically missing from any particular sol's 12 orbits, reducing the sol average to about 18,500 spectra (as opposed to about 40,000 if we could return all the data).

MGS's sun-synchronous orbit means that observations are taken near 2 PM and 2 AM local time in each half of the orbit. In fact, the precise local time an observation is taken depends on both the latitude and the season at which it is taken. These behaviors are demonstrated in Fig. 1. We have removed some data from our analysis near the poles as the local times of those observations are more than 2 h from the nominal 2 AM or 2 PM. As the seasons progress, the eccentricity of Mars orbit changes the local time of the equator crossing by 1 h from the nominal 2 AM or 2 PM. Aside from avoiding the extreme polar data, we have made no effort to correct for these effects.

With 12 longitudes covered every day at the nominal 2 PM and 2 AM times, one should be able to constrain time-invariant phenomena with zonal wavenumbers of up to about 5, once every day. Additionally, with the typical latitudinal coverage afforded in the data set, one could also constrain the meridional behavior of the atmospheric perturbations with about 1/4° resolution, although we have used significantly less than that (namely 4° latitudinal resolution).

2.2. Spectra

The TES instrument, principally a Michelson interferometer, obtains spectra from 200 to 1600 cm^{-1} (6.25 to 50 μm) with a nominal resolution of 10 cm^{-1} or, less frequently in this data subset, 5 cm^{-1} (Christensen et al., 1992, 2001). While the instrument was designed to obtain spectral information about the mineralogy on the surface of Mars, it was also designed to exploit the fact that it looks through Mars' atmosphere in wavelengths where it is not transparent, and hence is used to study the atmosphere itself. Specifically, the CO_2 that composes the bulk of Mars's atmosphere has a strong absorption centered near 15 μm. By examining the wavelength dependence of observed radiance between the center and wings of that absorption band, information about the vertical structure of Mars atmospheric temperature can be obtained (Conrath et al., 2000; Smith et al., 2001). Using other features in the TES spectra, there is also information about dust (Smith et al., 2000), water vapor (Smith, 2002), and water ice (Pearl et al., 2001), although this study does not directly concern itself with those results.

2.3. Retrievals

We used temperature profile retrievals produced by the TES team; see Conrath et al. (2000) for details of the algorithms used. The process of producing atmospheric temperature profiles from thermal infrared spectra is not trivial. While the emission from the core of the particular absorption feature corresponds to the temperatures at the highest levels in the atmosphere, and the wings are indicative of the lowest levels, the translation from radiance to temperature is not a simple mapping. Rather, the emission at a certain wavelength is indicative of the temperature over a range of pressures, with some inherent vertical smoothing. In addition to this vertical mixing of information (which is described by the "contribution function" of a particular wavelength), there is also the problem of noise in the observations. Conrath et al. (2000) used a least-squares approach to translate radiances into vertical temperature profiles, minimizing the differences between synthetic radiances from a retrieved temperature profile and the actual

radiances observed. They also applied a smoothness constraint on the retrieved temperature profile to reduce problems introduced by noise in the observations.

2.4. Limitations

Conrath et al. (2000) state that the systematic errors present in the retrieved temperature profiles could be as large as 5 K in the coldest places on the planet and less where it was warmer. However, they add that systematic errors less than about 2 K are also possible due to uncertainties in the CO_2 absorption coefficients. They further suggest that the random errors that result from their retrieval scheme in the presence of noise on the observations are typically of order 0.5K. Exceptions to this are locations where the assumed surface pressure is in error, yielding errors of up to 6K (for a 5% error in surface pressure) in the lowest scale height. However, all of the data used in this study was processed with improved surface topography data from MGS MOLA (Smith et al., 1999) which should have reduced the occurrence of significant surface pressure assumption errors.

The lowest layer (e.g., $\sim$1/2 scale height) in the atmosphere is often very difficult to retrieve accurately. This is partly due to the effect mentioned above, errors in the surface pressure assumption, but also partly due to the large contribution of surface radiance, making it difficult to disentangle the two sources of radiance. Furthermore because of the sharp temperature gradients that exist in the diurnal boundary layer, the retrievals will not faithfully reproduce the fine structure in the true temperature distributions. Because of these effects, we expect that the retrievals will have less accuracy in the lowest atmospheric layer ($\sim$1/2 scale height).

There is a limit to how high one can retrieve a temperature profile from a nadir spectrum. The wavelengths most opaque in CO_2 will have a maximum in their contribution functions at some finite pressure (about 0.5 mbar for 666 cm^{-1} at Mars at 10 cm^{-1} resolution; see Conrath et al. (2000) Fig. 1). While information can be obtained about the temperature structure some distance above this by exploiting the differences between adjacent wavelengths' contribution functions, the information content of the spectra is clearly limited above this height. Effectively, the TES nadir spectra have little information content above about 0.1 mbar (about 4 scale heights), and we will use that as the top of our analysis domain.

As mentioned above, using the nadir spectra of atmospheric absorption features for temperature structure retrievals introduces vertical mixing of information. This mixing, combined with the smoothing constraints imposed by the retrieval algorithm to limit the effects of noise in the data, results in a limitation on the vertical resolution of the retrievals. The vertical depth of the contribution functions combined with the smoothing lengths quantify this. For this relatively high-quality data set, the smoothing to control the noise is a secondary effect compared to the depth of the contribution functions, which are representative of the vertical resolution. A general rule of thumb is that for nadir spectra, contribution functions are roughly a scale height in depth. For this particular problem, Conrath et al. (2000) have presented some specific contribution functions in their Fig. 1. From this, we see that while contribution functions are about 1 scale height deep near the surface, they become deeper near the top of the domain ($\sim$ 0.5 mbar). Thus, the vertical resolution in the nadir temperature retrievals is about 1 scale height near the surface and perhaps almost 2 scale heights at a pressure of 0.5 mbar. This limitation has serious implications for our ability to resolve perturbations in the atmosphere with short vertical wavelengths.

3. Analysis approach

The goal is to sift through the roughly 12 million nadir temperature retrievals that were obtained during the first martian year of MGS's mapping mission and extract the forced oscillations that can be found in the data set. We already performed a similar analysis on the MGS TES data that was obtained during the mission phases before mapping (Banfield et al., 2000). However, in that analysis we focused on the tidal modes as that phase of the mission afforded good local time coverage for some latitudes. This analysis will emphasize the stationary waves, as longitudinal coverage is good, while time of day coverage is very limited (two local times only). However, there are other modes (various thermal tides) that will alias into our analysis and complicate the results.

A secondary goal of this analysis is to pave the way for a further analysis that will focus on transient waves. That analysis is more difficult than this, as no expected form for the waves can be assumed beforehand. That is, the forced waves have regular patterns that are, if not fixed in space, at least a well defined function of space and time. In contrast, the transient waves may move with a range of phase speeds, and be composed of a variety of zonal and meridional length scales. Because of these difficulties in knowing, a priori, what form and speed to assume for a transient wave, we will wish to remove all other effects before trying to isolate the transient waves. Principally, that means removing from the data set all of the regular perturbations that we can identify, essentially the focus of this study.

3.1. Binning

We have chosen to use a relatively simple approach, that of binning the data, to isolate the regular perturbations. The simplicity of the approach allows for a more understandable analysis, and appears to be appropriate for the task. The tradeoffs to be considered involve the bin sizes in the different dimensions. The offsetting factors are the resolution (smaller bins) versus the coverage and noise averaging (larger bins). The dimensions to be considered include the local time, pressure, L_s or season, latitude, and longitude.

For this data set, taken from the mapping orbit, the local time of the observations is basically either 2 AM or 2 PM, for all but the most polar observations. We use only these two local time bins and exclude observations that are more than a few hours from these nominal times. This cuts off a negligible latitude range from our analysis.

We used 8 bins in the vertical, each bin extending one-half of a pressure scale height, starting at 6.1 mbar, and extending to about 0.18 mbar, i.e., 6.1 mbar, 3.7 mbar, 2.2 mbar, 1.4 mbar, 0.8 mbar, 0.5 mbar, 0.3 mbar, 0.18 mbar. While there may be phenomena in Mars atmosphere with shorter vertical wavelengths than this, we certainly can't resolve them with the TES nadir temperature retrievals. The retrievals' analysis warrants no greater vertical resolution than this. In fact, we have oversampled the intrinsic resolution of the retrievals by perhaps a factor of four near the top of the domain.

We chose to bin the seasonal variable, L_s, by 30°, which is 1/3 of a season or about 60 sols. The desire to resolve seasonal changes drives this binning to smaller durations, while the need to discriminate between slowly moving transient waves and true stationary perturbations drives it to larger durations. Our results suggest that the seasonal changes (except perhaps during dust storms) are well resolved with L_s bins of 30° or less. Our preliminary experience with the transient waves suggests that some of them have periods of 20 sols or more, so the binning time should exceed 10° of L_s. Practically, we chose to use the higher of this range, to make the results more easily manageable, and except perhaps during dust storms, we lose essentially nothing with this seasonal binning.

In the latitude direction, we chose to bin by 4°. We have tried performing much of our analysis with 2° of latitudinal resolution, and the results were essentially unchanged. With 12 longitudinal bins, we can identify zonal modes up to about wavenumber 5. This should be sufficient for our analysis. For the perturbations of interest, power seems to drop off quite quickly with increasing zonal wavenumber in the Mars atmosphere; modes 0 through 3 are by far the most interesting.

The binning is performed on 2 local time bins, 1/2 scale height vertical bins (totaling 8), 30° L_s seasonal bins (~60 sols), 4° latitudinal bins, and 30° longitudinal bins (12 bins). This combination of bin sizes seems to retain as much information as possible in the data set, while still allowing for a manageable set of results. Once the data were segregated into the appropriate bins, we computed the average of all the data in each bin, yielding a multidimensional map of the temperature in Mars atmosphere as a function of local time, pressure level, season, latitude and longitude.

3.2. Averages and differences

There is information in the data set in both the average of the 2 AM and 2 PM observations and their differences. Averaging the observations is representative of their time independent behavior, while differencing them is representative of the diurnal variations. These sums and differences are our basic quantities of analysis. That is, we took the 2 AM and 2 PM bins and computed from them an average map and a difference map,

$$T_{\text{avg}} = (T_{\text{2PM}} + T_{\text{2AM}})/2, \tag{1}$$

$$T_{\text{dif}} = (T_{\text{2PM}} - T_{\text{2AM}})/2. \tag{2}$$

These two maps were then Fourier analyzed in longitude to yield amplitude and phase maps of different longitudinal wavenumber perturbations.

3.3. Wave modes and degeneracies

While the first-order interpretations of time-invariant and diurnally varying behavior are instructive in understanding the average and difference maps, they are not complete. In fact, the two maps are each composed of a set of terms, of which the first-order interpretations above are only the lowest order term. To see this, we start from the description of atmospheric perturbations as seen from a sun-synchronous spacecraft following that of Wilson (2000) (see also Forbes and Hagan, 2000). His Eq. (1) expresses the longitude–time dependence of stationary waves and thermal tides. If we generalize it slightly to recognize dependence on pressure and latitude, we have:

$$T(p,\,\phi,\,\lambda,\,t_{\text{lt}}) \sim \sum T_{s,\sigma}(p,\,\phi)\,\cos[(s-\sigma)\lambda + \sigma t_{\text{lt}} - \delta_{s,\sigma}(p,\,\phi)], \tag{3}$$

where p is the pressure, ϕ is latitude, λ is longitude, t_{lt} is the local time, s is the zonal wavenumber of the wave mode, and σ is the frequency (in sols^{-1}). T is the observed temperature, $T_{s,\sigma}$ is the amplitude of the mode defined by s and σ, and $\delta_{s,\sigma}$ is the phase of that mode. $\sigma = 0$ defines the set of stationary waves, while tides with $s > 0$ ($s < 0$) propagate westward (eastward). The sun-synchronous (migrating) tides are those where $s = \sigma$, leaving these modes only a function of local time for each pressure and latitude.

Note that we can write t_{lt} (2AM) + π = t_{lt} (2PM) = t_{2PM}. Thus, using this in Eq. (3), T_{2AM} is the same as T_{2PM} except for an additional $\sigma\pi$ in the arguments of the cosines. These additional $\sigma\pi$'s can be re-written as a multiplication of the cosines by $(-1)^{\sigma}$ instead. Thus, the expressions for temperatures observed half a sol apart differ only by the factor $(-1)^{\sigma}$ multiplying each term in the sums.

We can then form expressions for the T_{avg} and T_{dif} maps using the above simplification:

$$T_{\text{avg}}(p,\,\phi,\,\lambda) \sim \frac{1}{2}\sum_{s,\sigma}(1 + (-1)^{\sigma}) \times T_{s,\sigma}(p,\,\phi)\cos[(s-\sigma)\lambda + \sigma(\text{2PM}) - \delta_{s,\sigma}(p,\,\phi)], \tag{4}$$

$$T_{\mathrm{dif}}(p, \phi, \lambda) \sim \frac{1}{2}\sum_{s,\sigma}(1 - (-1)^{\sigma}) \times T_{s,\sigma}(p, \phi)\cos[(s - \sigma)\lambda + \sigma(2\mathrm{PM}) - \delta_{s,\sigma}(p, \phi)]. \quad (5)$$

From these expressions, one can see that the σ odd terms in T_{avg} will disappear, and the σ even terms in T_{dif} will disappear, leaving us with:

$$T_{\mathrm{avg}}(p, \phi, \lambda) \sim \sum_{\sigma=even,s} T_{s,\sigma}(p, \phi)\cos[(s - \sigma)\lambda + \sigma(2\mathrm{PM}) - \delta_{s,\sigma}(p, \phi)], \quad (6)$$

$$T_{\mathrm{dif}}(p, \phi, \lambda) \sim \sum_{\sigma=odd,s} T_{s,\sigma}(p, \phi)\cos[(s - \sigma)\lambda + \sigma(2\mathrm{PM}) - \delta_{s,\sigma}(p, \phi)], \quad (7)$$

To connect back with the observations, the fact that we can observe T_{avg} and T_{dif} means that we can separate out the wave modes with σ even from those with σ odd, but we can do no better than this in the time domain. The average maps represent atmospheric perturbations with σ even, that is time invariant terms (stationary waves, $\sigma = 0$), semidiurnal tides ($\sigma = 2$), and still higher even harmonic tides. The difference maps represent atmospheric perturbations with σ odd, that is the diurnal tide ($\sigma = 1$), the terdiurnal tide ($\sigma = 3$), and still higher odd harmonic tides (Forbes and Hagan (2000), Wilson (2000, 2002)).

We can, however, Fourier analyze the T_{avg} and T_{dif} maps in longitude. In Eq. (6) and (7) above, the zonal wavenumber of each term in the observed temperature distributions is $m = |s - \sigma|$. Thus, for T_{avg}, the wavenumber m component of the observed temperature distribution at a particular pressure and latitude is the sum of terms with σ even, and $s - \sigma = -m$ or $s - \sigma = m$. Similarly, for T_{dif}, the wavenumber m component of the observed temperature distribution is the sum of terms with σ odd, and $s - \sigma = -m$ or $s - \sigma = m$. All of these various terms contribute to an observed temperature modulation of T_{avg} or T_{dif}. We can do nothing more to separate them from one another in the observations, they are degenerate with respect to these observations. The various combinations that are aliased onto one another is elaborated more fully for $m \leq 3$, and $\sigma < 3$ in Table 1.

Clearly there are many wave modes that will contribute to each zonal wavenumber for either of the T_{avg} or T_{dif} maps. Therefore, identifying which (if any) wave mode dominates each map is critical for the use of our results to constrain the behavior of that wave mode. With the data set considered in this work, we have no way of determining which among the degenerate wave modes dominate for a given zonal wavenumber; we have to turn to other work to evaluate that.

Table 1
Combinations of σ and s that contribute to each zonal wavenumber, m, component of the two types of maps, T_{avg} and T_{dif}

Zonal wavenumber	Map type	σ	s	Comments
$m = 0$	avg	$\sigma = 0$	$s = 0$	Zonal mean, steady
		$\sigma = 2$	$s = 2$	Semidiurnal sun-synchronous tide
	dif	$\sigma = 1$	$s = 1$	Diurnal sun-synchronous tide
$m = 1$	avg	$\sigma = 0$	$s = \pm 1$	Stationary wave
		$\sigma = 2$	$s = 1$	
			$s = 3$	
	dif	$\sigma = 1$	$s = 0$	Diurnal, zonally symmetric
			$s = 2$	
$m = 2$	avg	$\sigma = 0$	$s = \pm 2$	Stationary wave
		$\sigma = 2$	$s = 0$	Semidiurnal, zonally symmetric
			$s = 4$	
	dif	$\sigma = 1$	$s = -1$	Includes diurnal Kelvin Wave DK1
			$s = 3$	
$m = 3$	avg	$\sigma = 0$	$s = \pm 3$	Stationary wave
		$\sigma = 2$	$s = -1$	
			$s = 5$	
	dif	$\sigma = 1$	$s = -2$	Includes diurnal Kelvin Wave DK2
			$s = 4$	

This table only goes up to $m \leq 3$ and $\sigma < 3$. Stationary waves are so noted in the comments, and the zonal mean and particular thermal tides are also indicated. The terms without comments are all nonmigrating thermal tides.

3.4. Accuracy

We have estimated the accuracy with which we could constrain the amplitude and phase of a wave mode that remained steady over our $L_s = 30°$ averaging period. We created synthetic temperature distributions including meridional and vertical gradients in the mean temperature, various amplitude and wavenumber oscillations, and random errors. All of these parameters were chosen to roughly mimic the real observations. We estimated the random noise of the retrievals to be between 1K and 3K. Conrath (2000) suggests that 1K might be accurate, but 3K is certainly a conservative estimate. The effect of this magnitude of random retrieval error over our long averaging period and the many observations included is quite small. Amplitudes were recovered with errors of less than 0.1K, while the accuracy of the phase estimates is inversely proportional to the amplitude of the wave mode. Specifically, we found a rough relation of $\delta\phi \sim 2/(m \times \text{amplitude})$, where amplitude is in degrees K and $\delta\phi$ is in degrees of longitude. Effectively, this means that for an $m = 1$ wavemode amplitude of 1K, the error in the phase estimate is about 2° of longitude. These results suggest that our long averaging period and the wealth of TES retrievals with relatively small errors allow us to constrain the amplitude and phase of the wave modes quite accurately. However, our synthetic retrievals were steady over time, and the real atmosphere may not be so well behaved. With this in mind, our results are indicative of a time average of a given wave mode over the period sampled, which certainly differs from instantaneous ampli-

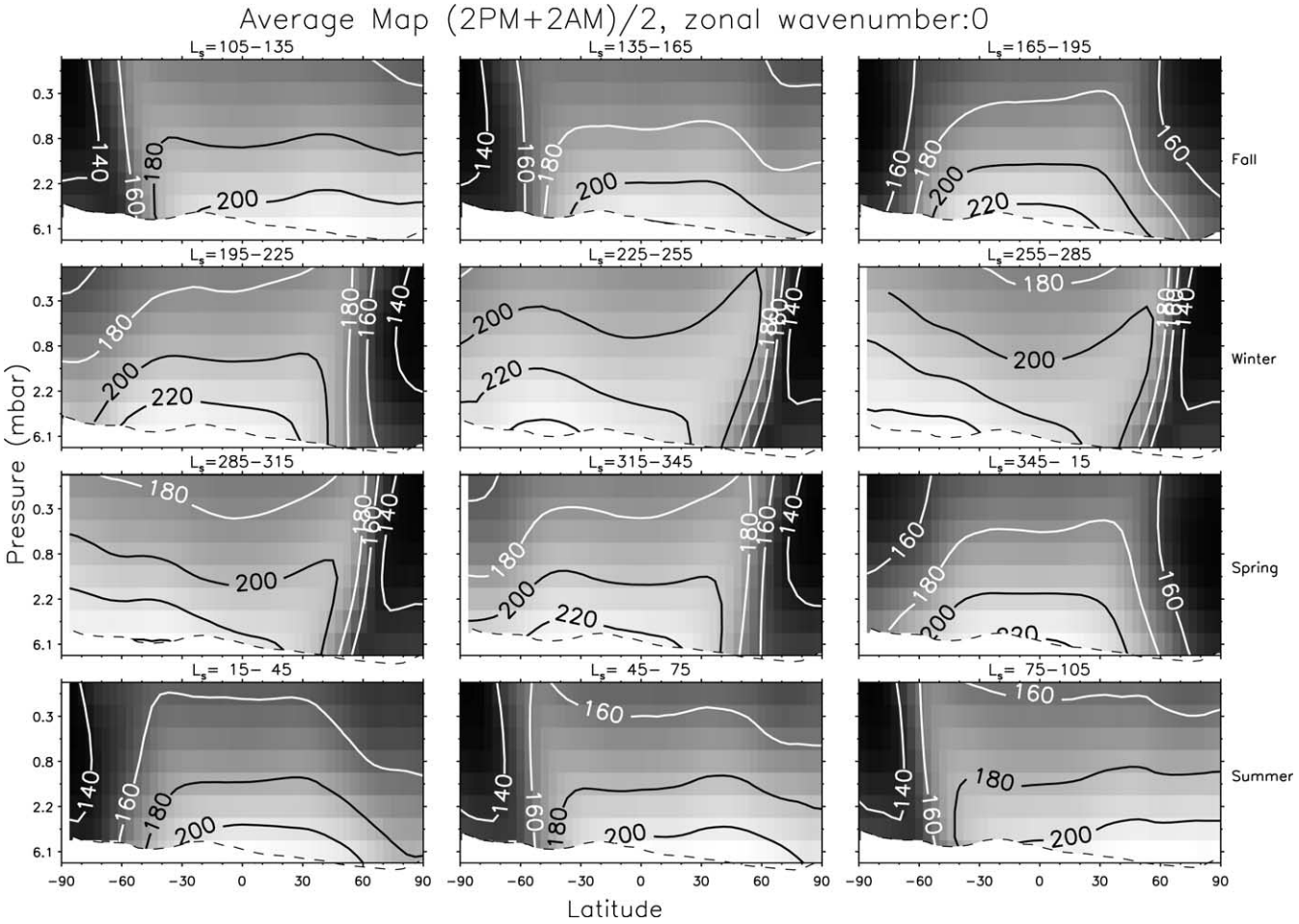

Fig. 2. Compound plot showing amplitude of the $m = 0$ average map ((2PM + 2AM)/2) as a function of latitude and pressure for a set of different ranges of season (L_s). The pressure levels indicated are 1-scale-height intervals above 6.1 mbar. An estimate of the zonal mean surface pressure (changing with season) is indicated by the blank region below the dashed line near or below the bottom of each plot. L_s (in °) is indicated above each panel. Northern fall is at the upper right, with winter, spring and summer below it, respectively. Contours are labeled in K, and brightness indicates high temperatures. These maps are dominated by the time average zonal mean temperature, but also include contributions from the semidiurnal tide and higher even harmonic sun-synchronous tides.

tudes. From experience with our results, we conservatively expect that observed amplitudes of about 0.5 K or greater are realistic, with phases accurate to within 10° of longitude.

4. Results

In this section, we present the various average and difference maps for zonal wavenumbers increasing from $m = 0$ to $m = 3$. We will discuss which wave modes are likely to dominate the different zonal wavenumbers, and discuss the agreement between this work and previous published analysis of these wave modes. The plots will all appear as compound plots, with 12 panels representing the different seasonal bins covering a full Mars year. Each panel of the compound plots is a latitude pressure map of the amplitude and phase of the given zonal wavenumber, either the average map or the difference map. The season or L_s range of each panel is labeled at its top. The rightmost column of each compound figure displays (northern) fall equinox, winter solstice, spring equinox, and summer solstice reading downward. Amplitude is indicated by contours, labeled in K, as well as in brightness. For the plots with zonal wavenumber not zero, phase is indicated by the color; each plot also contains a labeled color bar across the top to identify the phases. Regions where there was insufficient data to produce a reliable result were left blank white.

4.1. Average maps, $m = 0$

The first compound plot we present (Fig. 2) is the average maps with $m = 0$. These maps are dominated by the time average zonal mean temperature, s, $\sigma = 0$. However, they also have some contributions from the sun-synchronous semidiurnal tide (s, $\sigma = 2$) and higher even harmonic sun-synchronous tides. Banfield et al. (2000) find typical

values for the semidiurnal tide of about 2 K (range: 0–8 K) in the limited domain of their analysis (90S–30S), which unfortunately leaves out the tropics, where the semidiurnal tide is expected to be strongest. An MGCM simulation for $L_s = 235°$ with visible column dust opacity of about 1 produces a semidiurnal tide amplitude of ~2 K. Wilson and Richardson (2000) report model calculations that suggest equatorial semidiurnal tide amplitudes may reach as high as 10 K at altitudes of 25–35 km for high (about 5) column dust optical depths. Tide components with still higher even harmonics are significantly smaller and can likely be ignored (Banfield et al., 2000, Wilson and Hamilton, 1996).

We have no means of directly removing the semidiurnal tide and higher even harmonic tides from the $m = 0$ average maps to yield the true time average zonal mean temperature distribution. Neither is it feasible to accurately estimate this year's semidiurnal tide from earlier data; coverage is inadequate, and interannual variability is always an issue, especially with the semidiurnal tide's sensitivity to dustiness. If the average maps are taken as a proxy for the time average zonal mean temperature distribution, the errors associated with this are given roughly by the semidiurnal tide amplitudes, i.e., typically about 2 K, but perhaps as high as 10 K (if dustiness is high, Wilson and Richardson, 2000). Nevertheless, owing to the broad meridional structure of the dominant component of the semidiurnal tide, gradients in the zonal mean temperatures are likely the dominant terms in the $m = 0$ average maps. This suggests that gradient winds computed from the $m = 0$ average maps are likely quite accurate, as will be fields computed from higher order derivatives of these maps.

These maps, as proxies for the time average zonal mean temperatures, can be compared with the maps found in Conrath et al. (2000), derived from TES spectra from before the mission entered its mapping phase, and Smith et al. (2001) derived from the same subset of TES data as this work. Our results essentially reproduce those from Smith et al. (2001), with the notable difference in vertical extent. Smith et al. (2001) include limb retrievals in their analysis and thus can sample to 0.01mbar, nearly 3 scale heights higher than our work. Our results are significantly more complete in seasonal coverage than those of Conrath et al. (2000). The temperature cross sections from Conrath et al. (2000) compare very favorably (with one exception noted below) with those from this work, suggesting that interannual variations are small, well under 10K. Similar results are reported in Banfield et al. (2000), from the same data set as Conrath et al. (2000) (with a more complex approach, removing tidal aliasing) but have significantly reduced latitudinal coverage and resolution and are consequently more difficult to compare.

One difference between the temperature cross sections of Conrath et al. (2000) and this work does appear, comparing their Fig. 6, $L_s = 2°–4°$, with our results from $L_s = 345°–15°$. Our zonal mean temperature (proxy) shows much smaller latitudinal gradients throughout the tropics at this time. We checked to see if this difference resulted from our different averaging periods, but using their L_s limits did not remove the inconsistency. This is due to biasing in the observations that make up the Conrath et al. (2000) figure. Those data were from MGS before it entered its mapping orbit, and observations were biased toward morning at that season. The diurnal tide's amplitude and phase between the tropics and midlatitudes is such that morning observations of the tropics would be biased high relative to midlatitudes (e.g., Fig. 11 of Wilson and Richardson, 2000). Our T_{avg} observations, averaging two local times half a sol apart, are insensitive to the diurnal tide, and are also evenly sampled in longitude so other aliasing effects are minimized. If residual mean circulations were computed from the biased "zonal mean" temperatures from Conrath et al. (2000), one would incorrectly infer a reverse Hadley circulation to effect the apparent heating in the tropics. This demonstrates the possible consequences of using unevenly sampled maps of intricately varying fields.

4.1.1. Zonal mean zonal wind: $\bar{u}$

To facilitate discussion of the atmospheric regions with various wave propagation characteristics, we now compute the baroclinic component of the zonal mean zonal wind from the $m = 0$ T_{avg} map as a proxy for the time average zonal mean temperature. Because of the strong meridional temperature gradients in Mars' atmosphere, which induce strong zonal winds via sloping pressure surfaces, the Rossby number occasionally approaches or exceeds 1. This means that the inertia terms are at least of order the coriolis terms in the momentum balance. Thus we have had to use gradient wind balance, taking account of both coriolis and centrifugal terms to balance thermally induced pressure gradients. Note that while we can still calculate the balanced zonal winds, geostrophy and its associated theoretical machinery are not strictly valid in certain regions in the atmosphere. To compute the zonal mean zonal winds (Fig. 3), we have assumed a zero wind at 7.36 mbar (essentially at the surface), which effectively ignores any barotropic component of the wind field. This is a limitation that we must live with, as the barotropic component of the wind is unavailable to our observations. This analysis is very similar to that in Smith et al. (2001), with the differences being more complete seasonal sampling in this analysis but lower altitude sampling because of the nadir spectra only restriction.

The most striking feature in these plots is the winter polar jets. These strong eastward jets reach their maximum strength at winter solstice in both hemispheres, although the northern polar jet is notably stronger. It peaks at about 180 m/s while the southern jet peaks at about only 130 m/s. Both have their maxima above ~60° latitude and at the top of this domain. From this data alone, we cannot tell whether the winds continue to increase above this domain. However, Smith et al. (2001), using limb retrievals, showed that the polar jets reach their maxima at or just above the top of our

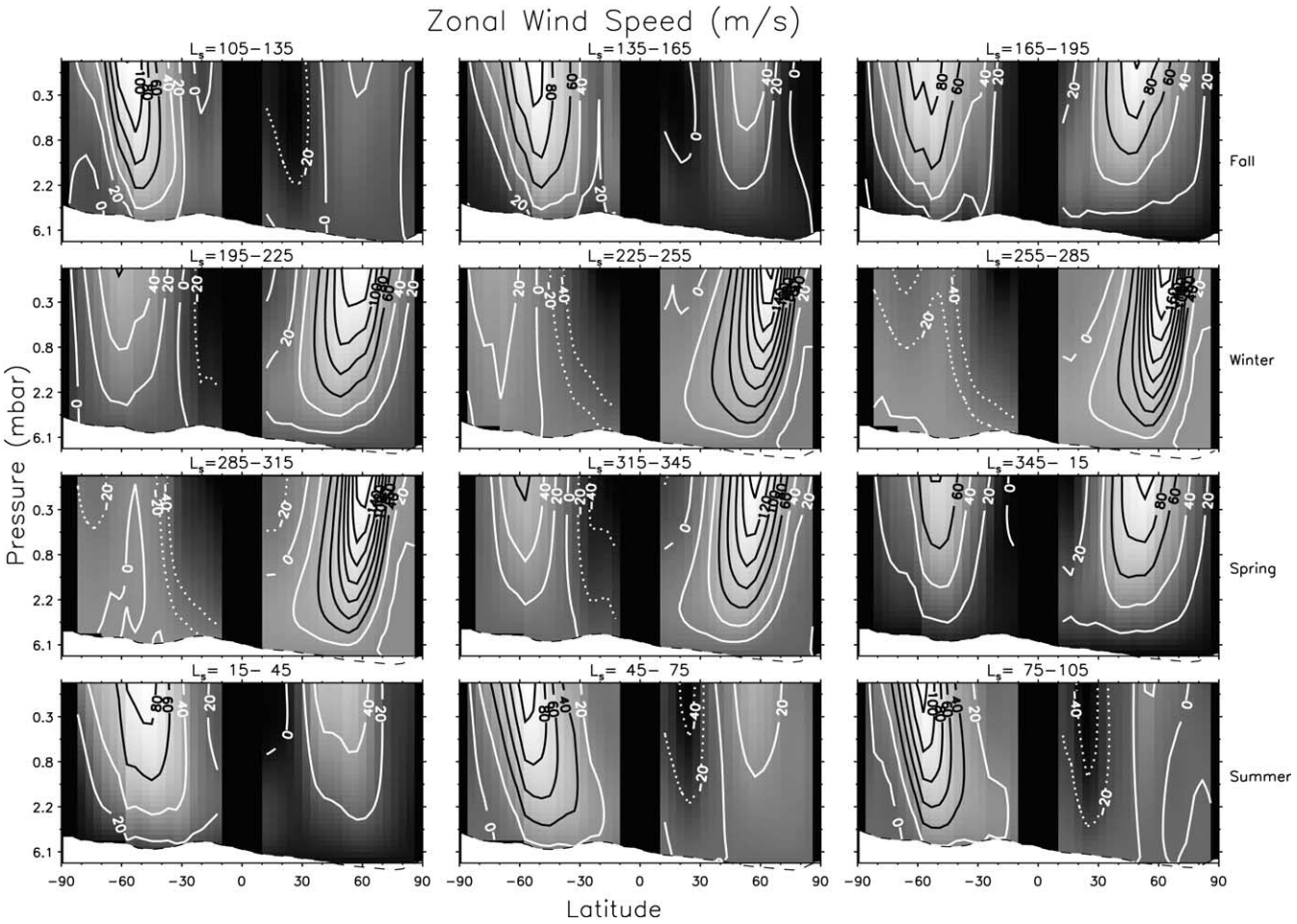

Fig. 3. Gradient wind balanced zonal mean zonal winds. This figure is of the same format as Fig. 2, with season progressing to the right and then down, L_s labeled (in degrees) above each panel. We have assumed zero wind at 7.36 mbar (essentially at the surface), and contours are labeled in m/s, with eastward winds positive. Negative (westward) winds have dotted contours. The shading is bright for the strongest westerlies in each panel and dark for the strongest easterlies in each panel. The equatorial region is blanked out because gradient wind balance breaks down there. Note the strong eastward jets located above about latitude 60° in the winter hemispheres. The northern winter jet is stronger peaking at about 180 m/s, while the southern jet peaks at about 130 m/s in this domain.

domain, near about 0.07 mbar, with maximum winds roughly the same as those found in our analysis. It is in these strong jets that centrifugal forces become significant, simple geostrophic balance is not accurately held in their cores. They are also the sites of the low-zonal-wavenumber stationary wave ducts that will be shown in the data and discussed more fully using the quasi-geostrophic index of refraction later in this work. In the summer tropics, away from the winter polar jets, we find westward jets near the top of the domain. Their amplitudes are about 40 m/s in the north and 110 m/s in the south, although error bars are large for tropical winds, as the calculation involves a division by the coriolis parameter which is small in the tropics.

In the equinoxes, nearly equal and symmetric eastward winds are evident in both hemispheres. These winds also grow with height to the top of our domain, peaking again at about 60°S, but slightly more equatorward at 50°N for the northern hemisphere. The wind speeds are notably smaller than the winter polar jets, of order 90 m/s. Smith et al. (2001) also showed that these equinoctial jets have a maximum at or just above the top of our domain, again near about 0.07 mbar, with maximum speeds again roughly the same as those found in our analysis. The latitudinal width of these equinoctial jets are much broader than the winter polar jets. The result of the smaller wind speeds and the broader extents is that the wind (and vorticity) gradients are much reduced in the equinoctial jets. This has implications for wave ducting which will be made more evident with later diagnostics.

4.2. Quasi-geostrophic index of refraction

Going beyond the zonal winds, quasi-geostrophic indices of refraction are of relevance to the stationary waves that we will extract from the data. Andrews et al. (1987) has a discussion of the application of the indices of refraction to

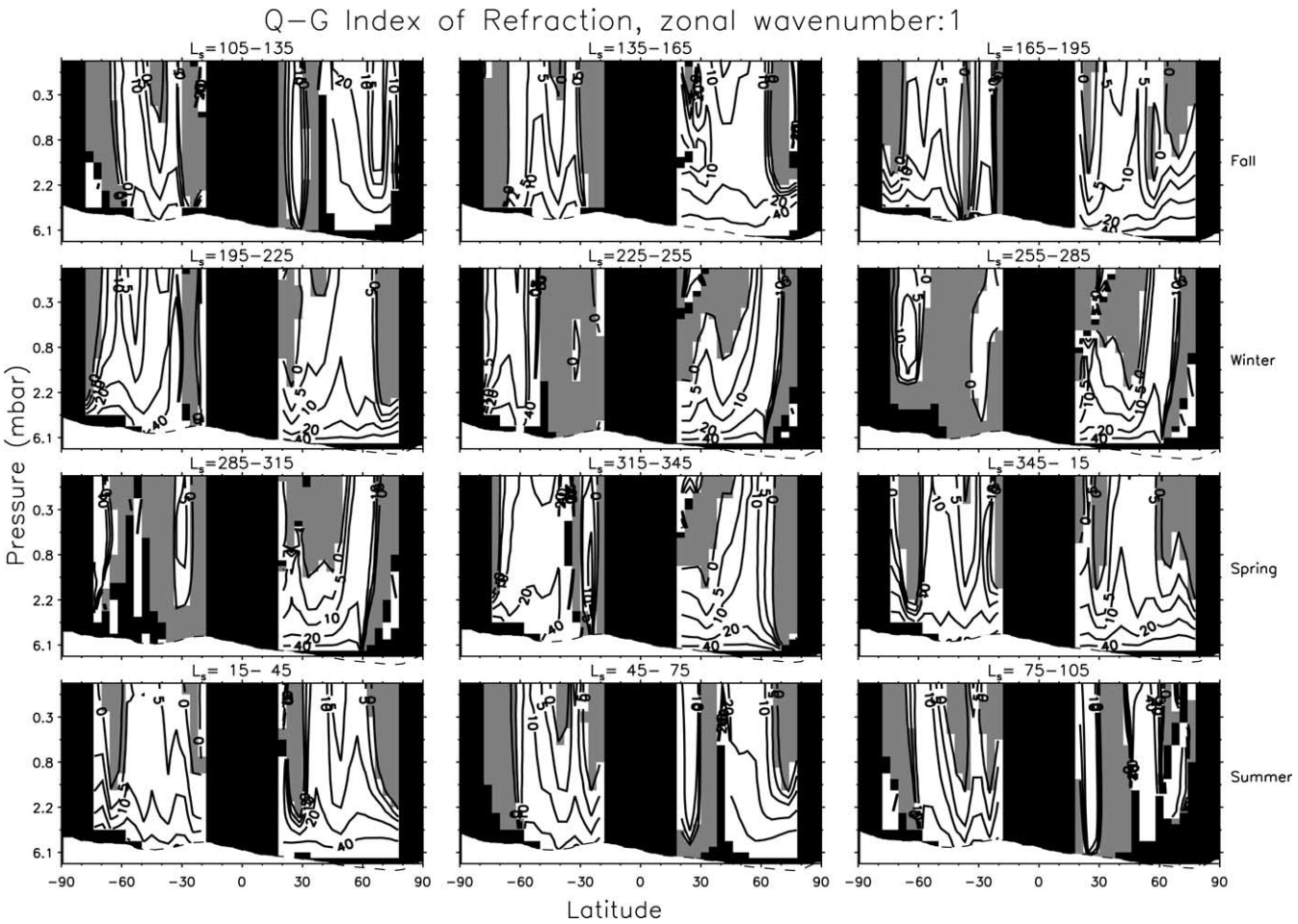

Fig. 4. Quasi-geostrophic index of refraction, $s = 1$ stationary wave. Values are normalized by $0.01\Omega/r$, where Ω is the planetary rotation rate. Only positive contours are shown, indicating regions where stationary wave propagation is expected. Negative indices of refraction are shown as grey, and regions where the index of refraction could not be calculated are shown as black. The winter polar jets form a large duct for this stationary wave mode.

understand wave propagation in the atmosphere. Of interest to our discussion is simply that regions of positive index of refraction can support wave propagation, while wave behavior will be evanescent outside of those regions. This can result in a duct for stationary waves, enhancing their amplitude in some regions of the atmosphere and excluding them from others. Armed with these estimates of the propagation regions, we can compare with the data to assess the self-consistency of our results. We use the expression from Palmer (1982) for the index of refraction, Q,

$$Q = \bar{q}_y/|(\bar{u}) - \left(\frac{s}{r\cos(\phi)}\right)^2 - (f/2HN)^2, \qquad (8)$$

where $\bar{q}_y$ is the meridional gradient of the zonal mean potential vorticity, $\bar{u}$ is the zonal mean zonal wind, r is the planetary radius, ϕ is the latitude, f is the coriolis parameter, H is the scale height, and N is the Brunt–Vaisala frequency. Again the caveat that geostrophy is not accurate in the cores of the zonal jets or near the equator applies, but outside of those regions, the results should still be accurate.

Fig. 4 shows the index of refraction for the $s = 1$ stationary wave for all the seasons in the TES data. Of note in this figure are the deep regions of large positive index of refraction along the cores of the winter polar jets. These form ducts that allow the $m = 1$ stationary wave to propagate up to high altitudes in these jets. These ducts are most pronounced near winter solstice and decay away from that season, moving equatorward and closer to the surface. In the winter hemispheres, the index of refraction also permits meridional propagation near the surface, which may allow stronger topographic forcing at lower latitudes to influence the waves found in the ducts at higher latitudes. In the summer hemispheres, the propagation regions are generally isolated well above the surface, suggesting that the effects of topographically forced waves are small there. During the equinoxes, there are substantial regions of positive index of refraction extending from the surface up to above 4 scale heights, but these differ from the winter polar vortex ducts by the relatively small values of the index of refraction for altitudes above about 1.5 scale heights. Upward propagating waves in regions of small index of refraction are more subject to absorption compared with regions of large index

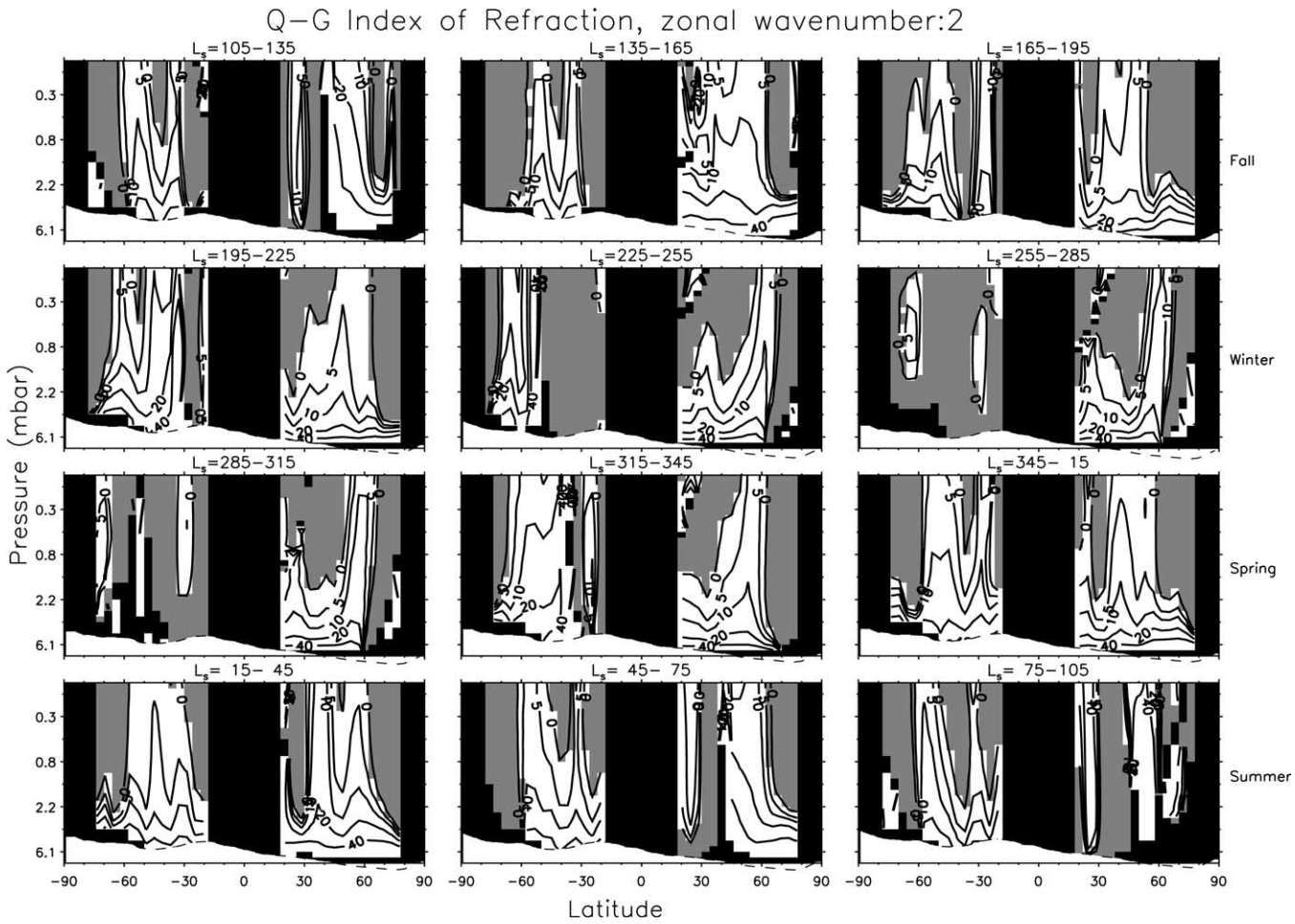

Fig. 5. Quasi-geostrophic index of refraction, $s = 2$ stationary wave. This plot is the same as Fig. 4, except for the $s = 2$ stationary wave. Notice the reduced extent of the winter polar jet duct.

of refraction. Thus, we might expect stationary waves to be significantly smaller in the equinoctial propagation regions than in the winter polar ducts.

Fig. 5 shows the index of refraction for the $s = 2$ stationary wave. This wave has a significantly reduced region of propagation, but still exhibits the winter polar jet ducts like the $s = 1$ stationary wave. The ducts decay at lower altitudes than those for the $s = 1$ stationary wave.

Fig. 6 shows the index of refraction for the $s = 3$ stationary wave. Again, this has an even more reduced region of propagation, with apparent but sharply reduced winter ducts. In this case, the winter ducts are so strongly reduced that the index of refraction in them does not differ greatly from that found at midlatitudes during the equinoxes. As we argued for the equinoctial case with the $s = 1$ stationary wave, we expect that absorption may effectively destroy the winter polar duct for the $s = 3$ stationary wave. Hence, we might expect to find $s = 3$ stationary wave amplitude only significant near the surface at all times and latitudes. The index of refraction for the $s = 4$ stationary wave (not shown) has barely a remnant of the winter polar duct, and we expect there to be essentially no vertical propagation of topographically forced waves with this high of a zonal wavenumber.

4.3. Difference maps, $m = 0$

The difference maps with $m = 0$ (Fig. 7) are dominated by the sun-synchronous diurnal tide (s, $\sigma = 1$). They also include contributions from the higher odd harmonic sun-synchronous tides (e.g., s, $\sigma = 3$). Banfield et al. (2000) suggest that the diurnal tide alone explains $\sim 70\%$ of their observed variance, while all of their modes with frequency 3 sol^{-1} only explain $\sim 6\%$ of the variance. We have also used GFDL MGCM results to confirm the validity of this dominance of the diurnal tide over higher odd harmonics, including the strongly tidally forced tropics, where Banfield et al.'s (2000) coverage was severely lacking. With this concurrence, we have ignored all terms with $\sigma \geq 3$ for all of the maps in this work (not just this one).

Because we are only observing at two local times, the thermal tides are aliased and thus cannot be unambiguously characterized. The limited time coverage does not constrain the amplitude and phase of this tide response. To aid in

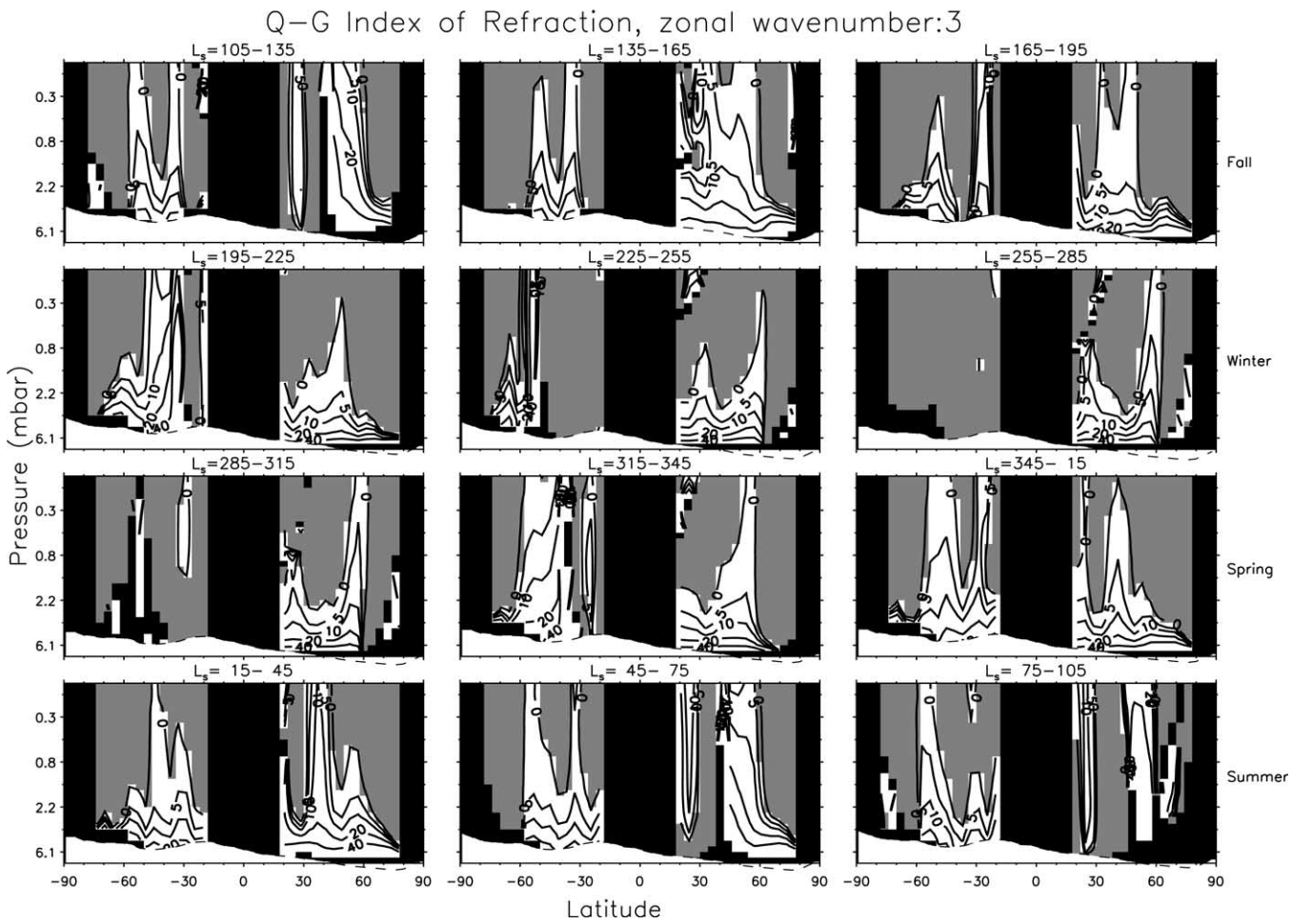

Fig. 6. Quasi-geostrophic index of refraction, $s = 3$ stationary wave. This plot is the same as Fig. 4, except for the $s = 3$ stationary wave. In this case, the winter polar duct is almost completely gone.

resolving this, we have used GFDL MGCM results to demonstrate the ambiguity as well as guide our scientific interpretations of the tide observations. The top panels of Fig. 8 show the simulated amplitude and phase of the diurnal tide for cases of low ($\tau \sim 0.4$, Fig. 8a, $L_s = 358°$) and moderate ($\tau \sim 1$, Fig. 8b, $L_s = 235°$) dust loading. The simulation employs an evolving dust source, yielding a dust distribution that is interactively controlled by the resulting atmospheric circulation (Richardson and Wilson, 2002). At $L_s = 358°$, the dust distribution is largely concentrated in the tropics. At $L_s = 235°$, the distribution is more uniform throughout the summer hemisphere. However, the results are not significantly dependent on the meridional dust distribution, rather, the total dust column and its vertical distribution are more important. The resulting zonal mean temperatures are in reasonable agreement with TES observations (Fig. 2). Figs. 8c and 8d show the corresponding (2PM–2AM)/2 difference fields, which may be compared with the observed tide fields in Figs. 8e and 8f. The TES fields represent 10-sol means (roughly 5° of L_s). The panel for $L_s = 235°$ corresponds to the period of maximum global mean temperature and tide amplitude following the onset of significant regional dust storm activity at $L_s = 225°$ (Smith et al., 2001). There is a reasonable correspondence in spatial structure and amplitude between the simulated and actual observations. Furthermore, they both share the same qualitative variation with season and dust loading. This accord between the data and model gives us confidence to use the MGCM as a guide with which to interpret the diurnal tide observations.

In the tropics, the simulated diurnal tide response (Figs. 8a and 8b) is dominated by a vertically propagating component with a vertical wavelength of about 33 km (Wilson and Richardson, 2000). This tide component is most prominent in the equinoctial seasons and is not simply dependent on dust heating. Its signature is clearly evident in the simulated difference field shown in Fig. 8c. Because the vertical wavelength is of the order of the vertical smoothing length of the TES nadir retrievals, the observed amplitudes are likely reduced from the actual atmospheric response. This smoothing is further exaggerated by the broadening of the weighting functions at the top of our domain and likely explains the differences between the observed and simulated temperature differences at $L_s \sim 358°$ (Figs. 8c and 8e).

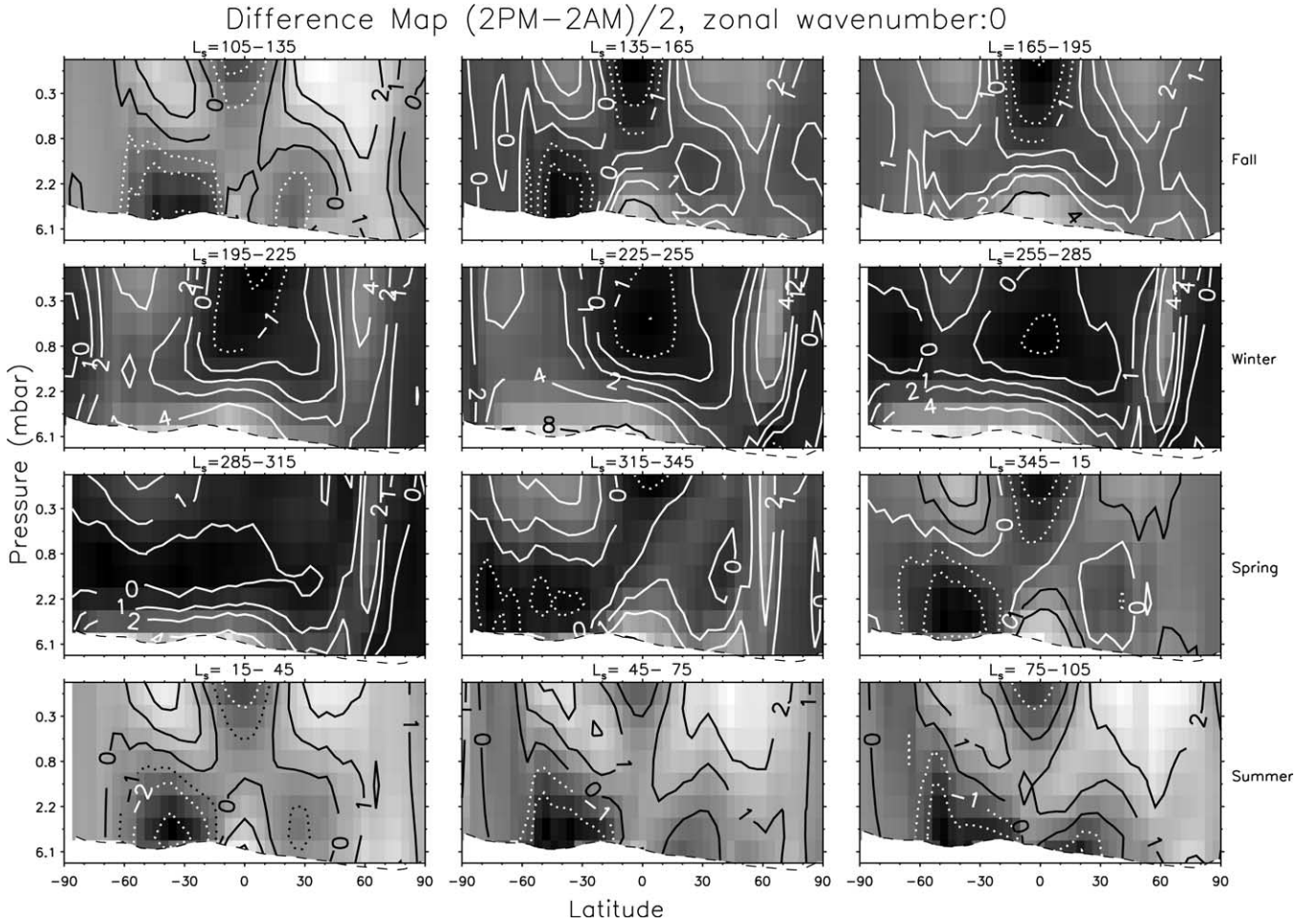

Fig. 7. Same format as Figure 2, but showing the distribution of the zonal mean ($m = 0$) difference maps (2PM–2AM)/2. Contours are again labeled in K, with dotted contours less than zero. Brightness indicates high positive values. These maps are dominated by the sun-synchronous diurnal tide, with contributions from higher odd harmonic sun-synchronous tides.

In particular, the simulation suggests a (2PM–2AM)/2 difference of approximately −7 K at 0.18 mbar, where instead we observe only about −3 K. Significantly, a preliminary analysis of TES limb retrievals in this season indicate a −8-K temperature difference, peaking at about 0.1 mbar. This suggests that vertical resolution must be considered in assessing vertical structure when significant phase variations are present.

Although the simulated tide amplitude continues to increase above 0.1 mbar, the (2PM–2AM)/2 field decreases just above this level as the phase regresses beyond 2AM. If the observations were shifted to different local times, they would show a similar peak at a different pressure level. This highlights the nonunique nature of inferring the diurnal tide amplitude and phase from our (2PM–2AM)/2 observations.

The $L_s = 235°$ simulation (Fig. 8b) indicates a significantly weaker tropical tide response that is somewhat ducted into the winter hemisphere. This tendency was noted in Wilson and Hamilton (1996) for solstitial conditions. A preliminary analysis of TES limb retrievals confirms that the upper level tropical diurnal temperature difference is quite weak (~3 K) during the solstice season and is notably displaced into the winter hemisphere in accord with Fig. 8d.

It is expected that a very large diurnal temperature variation should be present near the surface (e.g., Ryan et al., 1978). MGCM simulations indicate tide amplitudes of over 20 K at 100 meters above the surface, with the amplitude rapidly decreasing with height. Fig. 16 in Wilson and Hamilton (1996) shows the very shallow boundary layer response when the tide amplitude is calculated on a terrain-following vertical coordinate. When tide fields are constructed on constant pressure surfaces, as a consequence of large zonal variations in topography, they reflect the tide response at varying heights above the surface, leading to a smearing of the low-level temperature response. This accounts for the weak low-level tide response in Fig. 8a and 8b as the strong boundary layer temperature variations have been masked out by the highest topography along each latitude circle. This smearing, due to constant pressures corresponding to different altitudes, will also affect the TES observations, reducing their response to the boundary layer tide. The finite vertical resolution of the TES retrievals leads

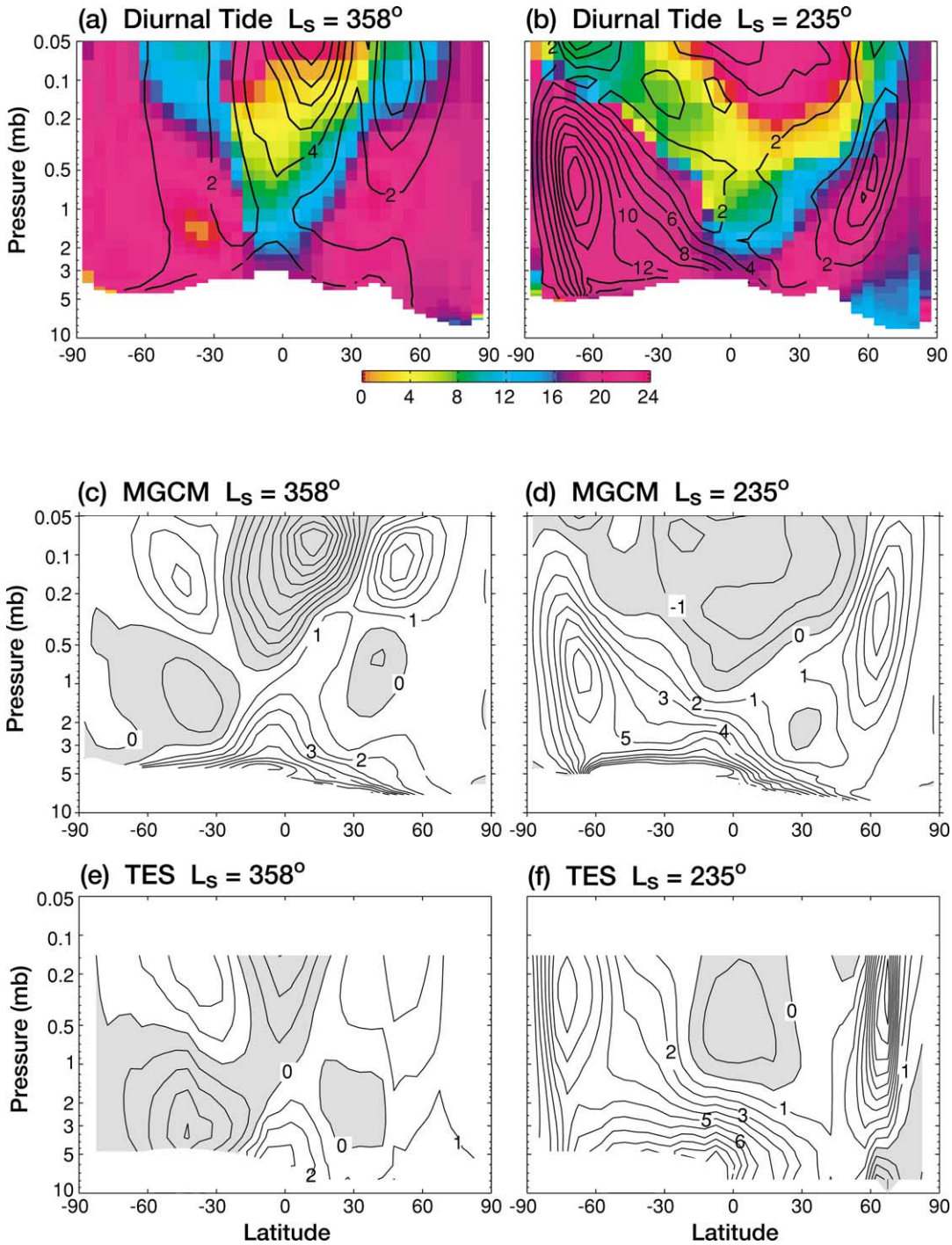

Fig. 8. Simulated diurnal tide amplitude and phase for (a) $L_s = 358°$ and (b) $L_s = 235°$. Tide amplitude is contoured at 2-K intervals while phase is indicated by color shading. Tide fields are calculated only for pressure levels that are entirely above the surface. The corresponding (2PM–2AM)/2 difference fields are plotted in panels (c) and (d). The contour interval is 1 K and negative regions are shaded. The observed TES temperature difference fields are shown in panels (e) and (f). The averaging interval for these maps is 10 sols (5° of Ls). Panel f corresponds to the peak of the dust storm activity that began at $L_s = 225°$.

to a further weakening of the near-surface tide estimate compared to that suggested by the MGCM simulations. It would appear that the boundary layer response is virtually absent in the TES data during periods of relatively low dust loading ($L_s \sim 330°$ to 180°) so that the observed low-level response is dominated by the vertically propagating tide component in the tropics.

By contrast, the extratropical tide response is characterized by relatively weak phase variation with height (the response is vertically trapped) and is thus expected to be

much more responsive to variations in dust heating (e.g., Wilson and Richardson, 2000). The temperature response peaks in late afternoon, roughly lagging the time of maximum heating by a quarter cycle (6 h). The differences in tide amplitude between Figs. 8a and 8b reflect the influence of greater solar heating by dust in the $L_s = 235°$ simulation relative to the $L_s = 358°$ simulation. The relatively deep and latitudinally broad temperature response extending upwards to 2 mbar that is evident in Fig. 7 during the ($L_s \sim 200°$ to 300°) season may be attributed to the enhanced dust heating in the lower atmosphere suggested by the dust opacity retrievals described by Smith et al. (2001).

Banfield et al. (2000) noted a persistent ($L_s \sim 180°$ to $L_s \sim 30°$) high amplitude (~8-K) diurnal temperature variation near the surface in the southern hemisphere, with a phase showing a maximum near local midnight. This is at odds with the results and expectations presented here. The Banfield et al. (2000) work is based on retrievals computed with pre-MOLA topography, which likely had significant errors in it. Conrath et al. (2000) caution that errors in surface pressure can manifest themselves as quite significant errors in the lowest scale height of the retrievals. All of the retrievals used in this study use surface pressure corresponding to MOLA topography and are thus much more reliable.

The dust storm that occurred at $L_s \sim 225°$ (Smith et al., 2001) has a definite effect on the diurnal tide amplitudes. This is most evident in the upper level tide response at $L_s \sim 235°$ (Fig. 8f), which is particularly prominent at rather high latitudes in both hemispheres. Note that differences between the simulated and observed temperature response (Figs. 8d and 8f) are likely due to an insufficiently deep dust distribution in the simulation. This comparison suggests that the observed extratropical tide field could be used to calibrate the solar heating due to dust in a dust storm simulation.

MGCM and linear model simulations (Wilson and Richardson, 2000) indicate that the summer high-latitude tide amplification is associated with the presence of high-latitude westerlies. The southern hemisphere westerlies weaken and vanish as the season progresses toward solstice (as the south pole warms), contributing to a weakening of the upper level tide response which tends to move equatorward to around 45°S, as suggested in the $L_s \sim 255°$–285° panel of Fig. 7. Of course the tide forcing is also weakening as well during this period. As the dust storm subsides, the maximum temperature differences at upper levels in the SH rapidly decline from a peak of 7 K at $L_s \sim 235°$ to 3 K at $L_s = 250°$, while the low-level tide amplitudes (below 1 mbar) decline much more slowly. The observed (2PM–2AM)/2 field may also be compared with that at the peak of the 2001 ($L_s = 205°$) dust storm that developed in the second year of MGS mapping operations (Smith et al., 2002). This storm also yielded the largest temperature differences at high southern latitudes, with values exceeding 20° K. Clearly this storm had much stronger dust heating than was present during the dusty period of the first mapping year.

The enhanced high-latitude response in Fig. 8 is also evident in Viking Infrared Thermal Mapper (IRTM) atmospheric temperature data for $L_s = 225°$ following the 1977a dust storm (Wilson and Richardson, 2000). The 1977a dust storm produced a high-latitude (~70°S) response in depth-weighted tide amplitude (centered at 0.5 mbar) that was significantly stronger than the tide response to the 1977b global dust storm, in spite of the fact that the latter storm was characterized by much greater radiative heating. The maximum tide response of the 1977b storm ($L_s = 285°$) was centered at ~45°S.

A region where 2AM temperatures are warmer than 2PM temperatures develops at ~ 1 mbar at $L_s \sim 275°$ and extends all the way to the surface by $L_s \sim 315°$ (Fig. 7). It is centered near the surface at southern mid-latitudes by northern spring equinox. This behavior persists until about $L_s \sim 155°$. MGCM simulations with various distributions of dust depth (not shown) indicate that there can be a notable phase shift in the summer hemisphere extratropical tide response at the top of a dust layer. This would suggest that the observations are consistent with a declining depth of the dust distribution in the southern hemisphere following solstice. Banfield et al. (2000) noted a similar situation, an apparent phase reversal of the diurnal tide above 2 scale heights in the summer south polar region following the Noachis dust storm. It seems likely that that was due to the same phenomena, the tidal phase changing abruptly above a sharply topped dust layer.

The simulated tide response in Fig. 8b is roughly consistent with the tide field deduced from aerobraking observations at $L_s = 235°$ following the Noachis dust storm seen in the previous Mars year (Banfield et al., 2000). Although the details of the dust activity around $L_s \sim 225°$ differed, the zonal-mean temperatures and opacities were quite similar (Smith et al., 2000, 2001) for the two years.

The large tide response at high latitudes in the northern hemisphere is not a consequence of in situ heating, but reflects the global nature of the tide response. The NH response is strongly localized along the polar frontal zone (Fig. 2). In this region, relatively small meridional displacements can be observed as relatively large temperature perturbations.

4.4. Average maps, $m = 1$

The $m = 1$ average maps (Fig. 9) are dominated by the $s = 1$ stationary wave ($\sigma = 0$), with contributions from several nonmigrating semidiurnal tides (e.g., $\sigma = 2$, $s = 1$ and $\sigma = 2$, $s = 3$). This conclusion is drawn in part from the expected amplitudes of the various modes that can contribute to these maps (see Table 1), but also from the expected vertical wavelengths of the significant modes. In this case, the two thermal tide modes that also contribute to these maps are expected to have smaller amplitude than the sta-

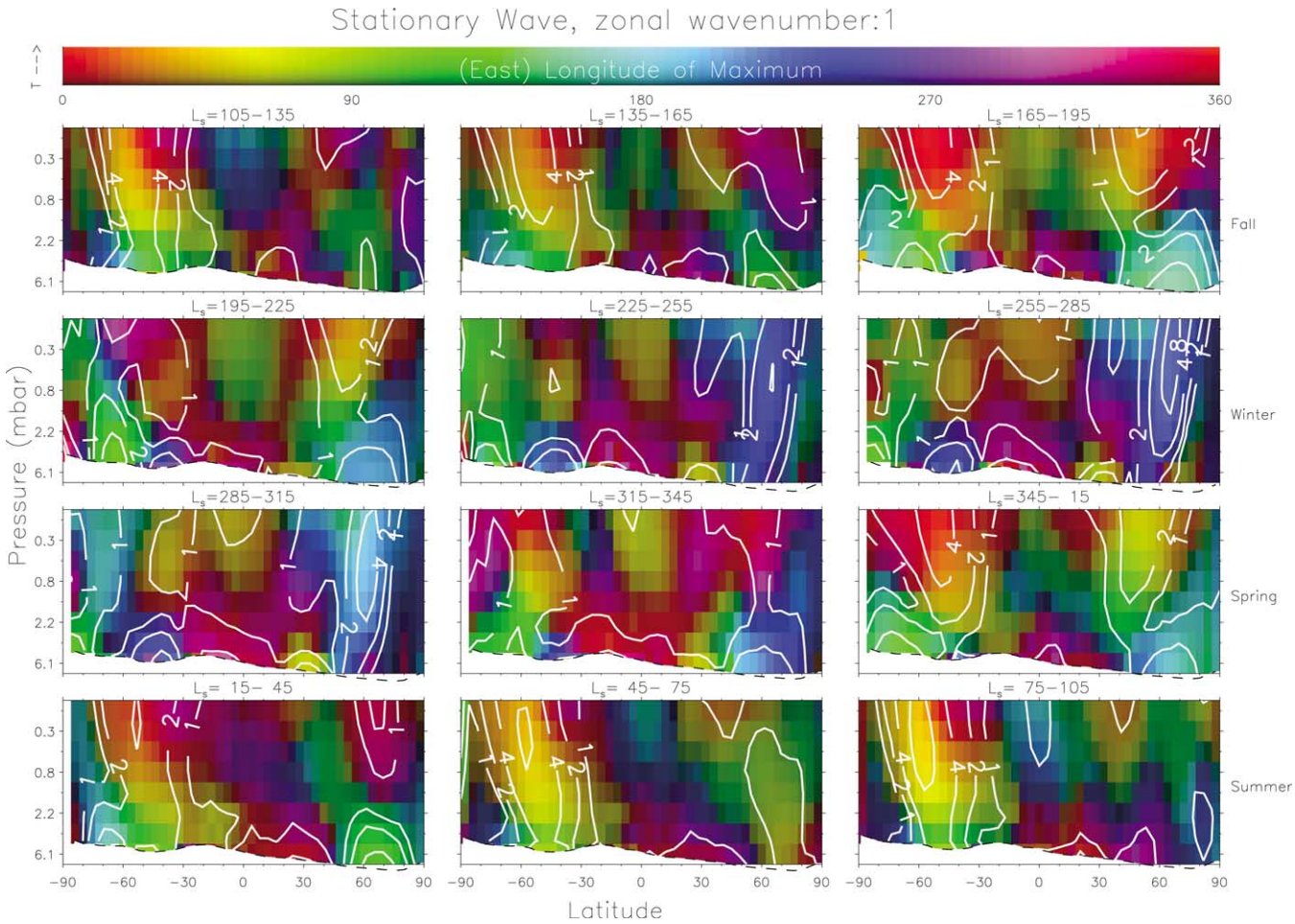

Fig. 9. Same format as Fig. 2, but showing the amplitude and phase (East longitude of maximum) of the ($m = 1$) average maps (2PM + 2AM)/2. Amplitude contours are again labeled in K, while phase is indicated by color with a color scale bar across the top of the plot. Higher color saturation also indicates higher amplitudes. These maps are dominated by the $s = 1$ stationary wave, with contributions from several nonmigrating semidiurnal tides. Fig. 4 shows the quasi-geostrophic index of refraction for this wave mode.

tionary wave, except for perhaps in the tropics where the tides are more strongly forced. There, the tides also will likely have a short vertical wavelength (less than ~30 km) and consequently be smoothed and partially attenuated by the vertical averaging of our observations. Hence, we conclude that these maps are dominated by the $s = 1$ stationary wave. This approach, considering the expected amplitude distribution of the various contributing modes and also their vertical wavelengths (and thus contributions after vertical smoothing), is what we use for the following maps as well. Expected tide amplitudes and vertical wavelengths are drawn from GCM modeling (e.g., Wilson and Hamilton, 1996) and linear tidal theory (e.g., Chapman and Lindzen, 1970).

The northern and southern winter mid-latitudes hold the highest amplitudes of the $s = 1$ stationary wave, with amplitudes reaching ~10 K. The southern winter stationary waves have a relatively steady phase behavior with latitude and altitude throughout winter. The maxima, slowly rising to and falling from 10 K around southern winter solstice, are found about 2 or more scale heights above 60°S. There is a notable westward phase tilt with height in the vicinity of the polar jet, with the longitude of the maximum at about 130°E near the surface, regressing to near 0°E by the top of our domain (see also Fig. 14). The regression is more rapid with height (the vertical wavelength is smaller) equatorward of the jet (i.e., at about 45°S), and slower poleward of 60°S. The longitude of the temperature maximum near the surface throughout southern fall, winter, and early spring (about 130°E) is about 90° west of the $m = 1$ component of topography at 60S (about 210E). By late southern spring and through summer, the southern midlatitude $s = 1$ stationary wave is confined to near the surface with amplitudes of 2–4 K, but is in phase with the topography in its vicinity (i.e., around 230E at 45S). The equinoxes are very similar to one another, with two local maxima of about 6 K, one 3.5 scale heights above 55°S, and the other near the surface poleward of 60°S.

The northern winter stationary waves have a slightly more complicated structure than those in the south. The

amplitudes are strongly peaked right at northern winter solstice, approaching 10.5 K then, but dropping to as small as 4–5 K 30° of L_s before or after. As in the southern winter, the high amplitudes are aligned along the polar jet axis, with the maxima about 2–3 scale heights above 65°N. In addition to the amplitude variation throughout the northern winter season, the complexity also comes in through the phase behavior of the $s = 1$ northern winter stationary wave. Between northern fall equinox ($L_s \sim 180°$) and when the polar jet duct forms (i.e., $L_s \sim 225°$), the wave maxima are found near the surface (~65°N), with the longitude of the maximum near 160°E. Above and slightly equatorward of these, secondary maxima are found near the top of the domain, with longitude of maximum moved westward with height to near 30°E. Similar behavior is also found during the northern spring equinox. When the polar jet duct forms (after $L_s \sim 225°$), the amplitudes grow, the maxima are found higher up, and the vertical structure becomes more barotropic. Phase differences between the top and bottom of our domain within the polar jet duct are less than or of order 20° of longitude, with the longitude of maxima near the surface about 230°E for $L_s = 225°$–315° (see also Fig. 13). When the polar jet duct is decaying, $L_s \sim 315°$–345°, the amplitude sharply decreases (~2 K) and is again confined mainly near the surface. The longitude of maximum remains near 210°E at the surface, tilting to the east with height. At the top of our domain, the longitude of maximum is at about 355°E for this period. The northern midlatitudes $m = 1$ component of topography is dominated by a maximum at about 260°E at about 40°N (basically Alba Patera) trending west to about 200°E by 60°N. The $s = 1$ stationary wave is in phase with the topography near the jet core (i.e., 45°N–60°N) during late northern fall and throughout winter, but about 90° west of it around the equinoxes, when the amplitudes are more confined near the surface. This behavior is opposite to that of the southern hemisphere $s = 1$ stationary wave, with the near-surface response 90° west of its $m = 1$ topographic forcing during the winter solstice when the amplitudes are large, but in phase with the forcing near the equinoxes when it is confined near the surface.

Hollingsworth and Barnes (1996) discuss how the $s = 1$ stationary mode may be near resonance in the northern winter, and varying jet strengths and shapes and dust distributions may strongly affect the amplitude of this mode. It is unclear how much this contributes to what we are observing in this data set. The amplitude goes through a sharp peak near the northern winter solstice, and the phase changes abruptly at the start and end of that growth. Our observed phase changes are consistent with the discussion in Barnes et al. (1996), who suggest that the $s = 1$ stationary wave may be longer than the resonant wavelength for times well away from the winter solstice and the thermal response would be found west of the forcing. They also suggest that during the solstice, the $s = 1$ wave may be at or near resonance, and the response should be in phase with the topography (as we observe). Both Hollingsworth and Barnes (1996) and Barnes et al. (1996) also discuss the effects of dustiness, working to bring the $s = 1$ stationary wave closer to resonance (all other things being equal). For this Mars year, dust opacity was at a maximum around $L_s \sim 240°$ (Smith et al., 2001), 30° of L_s before when we see the maximum stationary wave amplitude at the northern winter solstice. It is possible that the varying dust distribution influences the $s = 1$ stationary wave amplitude and phase distribution we have observed, but it appears simpler to ascribe it mainly to a seasonal change in the wave mode duct and forcing. Nevertheless, a near resonance of the northern $s = 1$ stationary wave seems consistent with the observations. It is unclear how to reconcile the southern $s = 1$ stationary wave behavior with resonant behavior. Because of all of this, the $s = 1$ stationary wave is apparently a sensitive benchmark with which to compare models, perhaps with many factors being tested simultaneously.

Barnes et al. (1996) (using Mars Consortium topography estimates, which differ considerably from MOLA topography data) note that the vertical structure of the $s = 1$ stationary waves is nearly equivalent barotropic (phase nearly constant with height) in their northern winter simulations, but has moderate westward phase tilt with height for the southern winter simulations. This agrees particularly well with our observations near the northern winter solstice, $L_s \sim 225°$–285°. For much of the time outside of this range of L_s, we see a westward phase change with height of the $s = 1$ stationary mode with a vertical wavelength of about 8 scale heights in the south and 16 scale heights in the north, in both cases depending on latitude (computed by extrapolating from the phase changes within our domain). Such a westward phase tilt with height is indicative of a baroclinic component of $\overline{v'T'}$. We will address this more fully later.

Concentrating only on $L_s \sim 75°$–105° and ~66°N (late northern spring to summer solstice) to compare with the results of Hinson et al. (2001), we find remarkably good accord. Their Fig. 11 shows amplitudes of order 1.5 K for $p >\sim 3$ mbar, about twice what we observe, but remember that our amplitudes may be somewhat reduced due to our inherent vertical smoothing. The phase of maximum for $p >\sim 1.5$–5 mbar is about 300°E in theirs and about 280°E in ours and for $p <\sim 2.5$ mbar it is about 120°E in both of our data sets. Note that these data sets are separated by 1 martian year, indicating good repeatability from year to year for the $s = 1$ stationary wave away from the dusty northern winter.

4.5. Difference maps, $m = 1$

We do not present this plot, as the amplitudes are all quite small (<3.5 K, typically ~0.5 K), only slightly above the noise, and there are no published structures with which to compare. These maps are likely dominated by the zonally symmetric diurnal tide ($\sigma = 1$, $s = 0$), but could also have contributions from the $\sigma = 1$, $s = 2$ tide. The zonally symmetric diurnal tide is forced by $s = 1$ topographic relief,

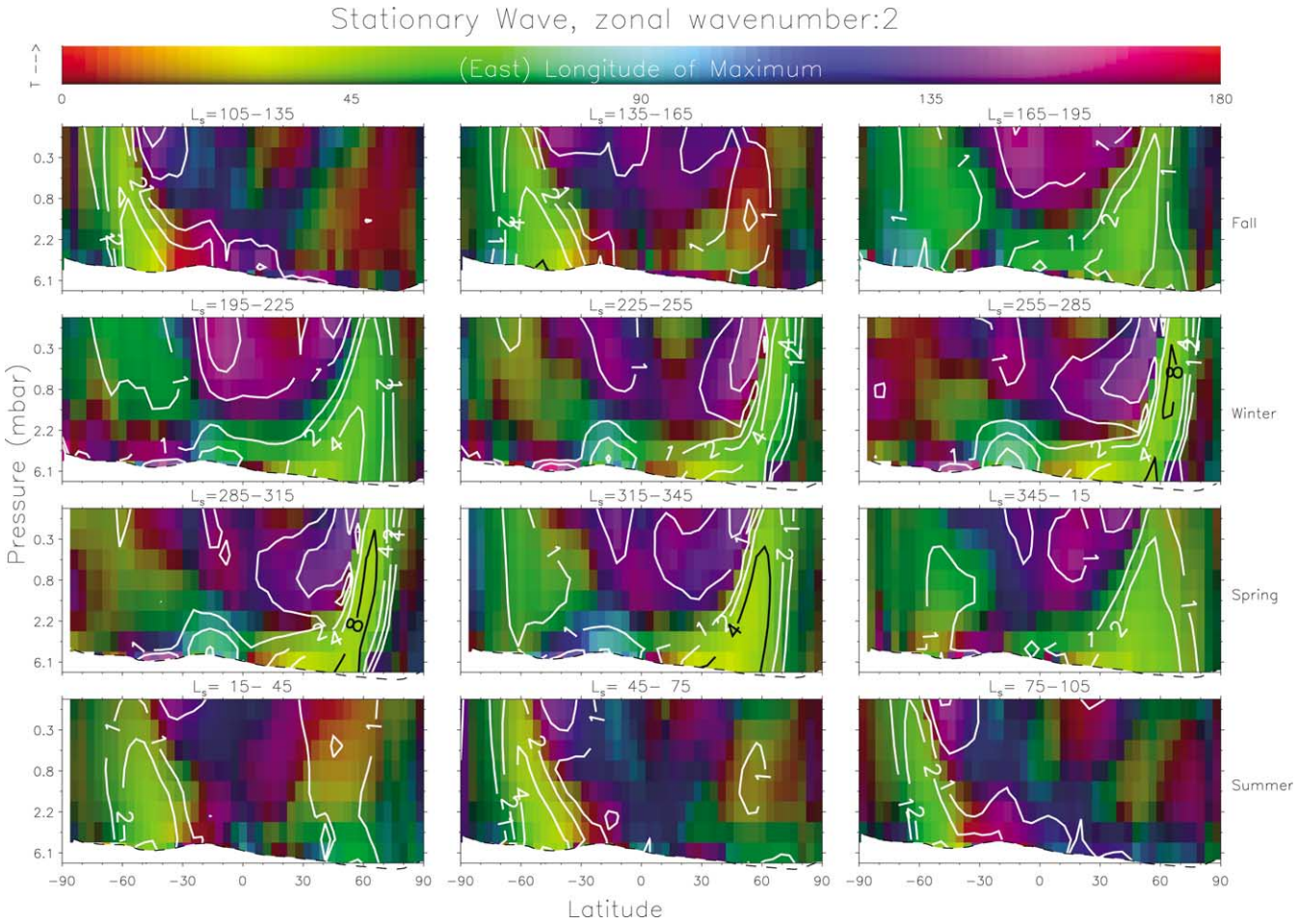

Fig. 10. Same format as Fig. 9, showing the amplitude and phase (East longitude of maximum) of the ($m = 2$) average maps (2PM + 2AM)/2. These maps are dominated by the $s = 2$ stationary wave, with contributions from a non-migrating semidiurnal tide, and the semidiurnal zonally symmetric tide. Fig. 5 shows the quasi-geostrophic index of refraction for this wave mode.

which contributes to a "breathing" of the atmosphere at all longitudes in phase with the heating over the high topography. With Tharsis, we might expect to find a maximum in 2PM–2AM at its longitude, about 260°E. The tropics of these maps show some suggestion of this, but the amplitudes are not large where the phase is consistent with this concept. More significant amplitudes of between 1 and 2 K are found in the lowest 2 scale heights above 40°S from $L_s \sim 315°$–135°, spanning northern summer. For these regions of relatively larger amplitude, the phase is consistently near 120°E, perhaps indicating the negative relief of Hellas as the cause.

4.6. Average maps, $m = 2$

The $m = 2$ average maps (Fig. 10) are dominated by the $s = 2$ stationary wave ($\sigma = 0$), but also have contributions from a nonmigrating semidiurnal tide ($\sigma = 2$, $s = 4$) and the semidiurnal zonally symmetric tide ($\sigma = 2$, $s = 0$). In this case, experience with GCM results suggests that the amplitude of the non-migrating semidiurnal tides are insignificantly small (<2 K) in comparison with the stationary waves (of order 4 K). The $s = 2$ stationary mode is remarkably steady in phase throughout the year, essentially remaining unchanged. However, its amplitude does significantly change with the largest found in the winter hemisphere, aligned along the polar jet.

The $s = 2$ stationary wave reaches an amplitude maximum of about 8 K in the southern winter hemisphere, at about 6 mbar over 50°S. The maximum amplitudes are actually found about 45° of L_s before and after the southern winter solstice, with the solstice itself a relative minima in amplitude. Amplitudes then decay again in the south as the season progresses to equinox only to grow in the north as winter approaches there. Amplitudes of over 8 K are reached at all but the top of our domain above 60°N during the northern winter solstice, with the absolute maximum occurring just after the solstice. Similarly to the south, the northern winter $s = 2$ stationary wave region of large amplitude narrows as winter solstice approaches (and amplitude grows), and then it broadens again as winter passes. The $s = 2$ stationary wave appears to slosh back and forth

very symmetrically following the winter hemisphere, with only a slightly larger region of high amplitude in the north. Outside of the polar jets, the amplitudes are of order 1–2 K throughout all of the year.

We can compare these amplitudes and spatial distributions of the $s = 2$ stationary wave with those from Fig. 9 of the $s = 1$ stationary wave. During southern winter, the $s = 2$ wave dominates only in late winter ($L_s \sim 135°$–$165°$) at the lowest two scale heights above about 50°S. Essentially for all other southern latitudes and seasons, the $s = 1$ wave dominates or is at least comparable in amplitude to the $s = 2$ wave. This dominance of the $s = 1$ stationary wave for the southern hemisphere was previously noted by Banfield et al. (1996) from Viking IRTM T15 data analysis for $L_s \sim 0°$, although that analysis used uncorrected T15 temperatures (Wilson and Richardson, 2000). They also noted that $s = 2$ dominated the northern hemisphere in their analysis. We find the same to be generally true in our analysis for the north, although it appears that $s = 1$ is occasionally of greater amplitude than is $s = 2$ near the top of our domain and north of the polar jet. The $s = 1$ wave has maxima in the northern winter at altitudes above 1 mbar, while the $s = 2$ wave has maxima typically near or below this altitude. Thus, while IRTM T15 may have seen $s = 2$ dominate in the north, the TES instrument with sensitivity to higher altitudes finds $s = 1$ dominating at the highest altitudes in northern winter.

Inside the winter polar jet ducts for the $s = 2$ stationary wave, the phase of the wave is almost constant with altitude, season, and for both the northern and southern hemispheres. Our analysis shows a maximum at about 45°E in the jets, with a nearly barotropic structure throughout the year. The wave in the southern winter polar jet shows a slight westward phase tilt with height. These phase distributons are consistent with the $m = 2$ component of the topography throughout the tropics and the northern midlatitudes controlled by the position of Tharsis and Olympus Mons. This tropical and northern midlatitude topographical forcing seems to control the $s = 2$ stationary wave in the southern jet as far south as ~75°S latitude as well. Outside of the jets, there is also a very consistent phase behavior. Where the amplitude sharply drops high in the jets, the phase undergoes a shift of π or about 90° of longitude. This is likely associated with the evanescent wave beyond the edges of the propagation region of this wave mode, i.e., beyond the edges of a duct.

The regularity and uniform behavior of this stationary wave makes it a valuable benchmark for modeling comparisons. Previous modeling works have only presented geopotential estimates, but for barotropic conditions, temperature perturbations are proportional. Hollingsworth and Barnes (1996) found both the $s = 1$ and $s = 2$ stationary waves were ducted into the winter polar jet. They also found a similar dominance of the $s = 1$ wave throughout the south and at higher altitudes in the north. Their model showed an equivalent barotropic structure for the $s = 2$ wave, in agreement with our results. However, the phase of the $s = 2$ wave in both hemispheres is off by about 50° of longitude between our analysis and their modeling, with their maxima east of ours. This may be due to their topography, which was based on pre-MOLA (Mars Consortium) estimates. Barnes et al. (1996) found a very similar amplitude and phase distribution as Hollingsworth and Barnes (1996) and also this work, with better accord between their models and our observed phase (their figures show phases of about 40°E for the northern winter $s = 2$ stationary wave, similar to what we found). Finally, Nayvelt et al.'s (1997) linear modeling also showed similar stationary wave results for $L_s \sim 270°$, with $s = 2$ dominating in the north, and also good phase consistency with our results. Note, however, that all of the modeling efforts published to date have used pre-MOLA topography.

4.7. Difference maps, $m = 2$

The $m = 2$ difference maps (Fig. 11) are dominated by the diurnal Kelvin wave ($\sigma = 1$, $s = -1$) (DK1), but also have contributions from a nonmigrating diurnal tide ($\sigma = 1$, $s = 3$). In this case, the vertical wavelength of the diurnal Kelvin wave is large, while that of the westward nonmigrating diurnal tide is small (< 30 km in the tropics). Because of the vertical smoothing of our data, and the likely small amplitude of this nonmigrating westward tide mode ($\sigma = 1$, $s = 3$), it is attenuated to the point of being insignificant in these maps. On the other hand, the diurnal Kelvin wave, with its large vertical wavelength, suffers no attenuation in the observations and dominates these maps. Note that the diurnal Kelvin wave DK1 was already identified in the MGS TES data by Wilson (2000) and also inferred to exist in the upper atmosphere of Mars from MGS accelerometer data by Forbes and Hagan (2000) and Wilson (2002). Seasonal changes are very minor in the maps, and amplitude is concentrated over the tropics, consistent with a Kelvin wave. The typical structure appears to be an amplitude of ~1–2 K, with a phase of the maximum at about 40°E throughout the southern tropics at altitudes above about 0.8 mbar lasting throughout the year, perhaps stronger in spring and fall. Then, throughout the tropics at altitudes below about 2.2 mbar is another local maximum of about 3 K with a phase again near 40°E that is most evident during northern fall and early winter ($L_s \sim 165°$–$315°$). There is also a suggestion of a local maximum in the lowest half scale height of the retrievals near 38°S. This local maximum is as high as 3 K, with a rough longitude of the maximum near 150°E. It is quite noisy, and evident almost only at the lowest scale height, suggesting that it might be a retrieval artifact. This overall structure persists throughout the year, with only minor changes in the amplitude and phase structure. At L_s ~255°–285° a region of higher amplitude directly in the northern polar jet core appears, with an amplitude of ~2 K and a phase of about 150°E. This region is probably not associated with the Kelvin wave and may

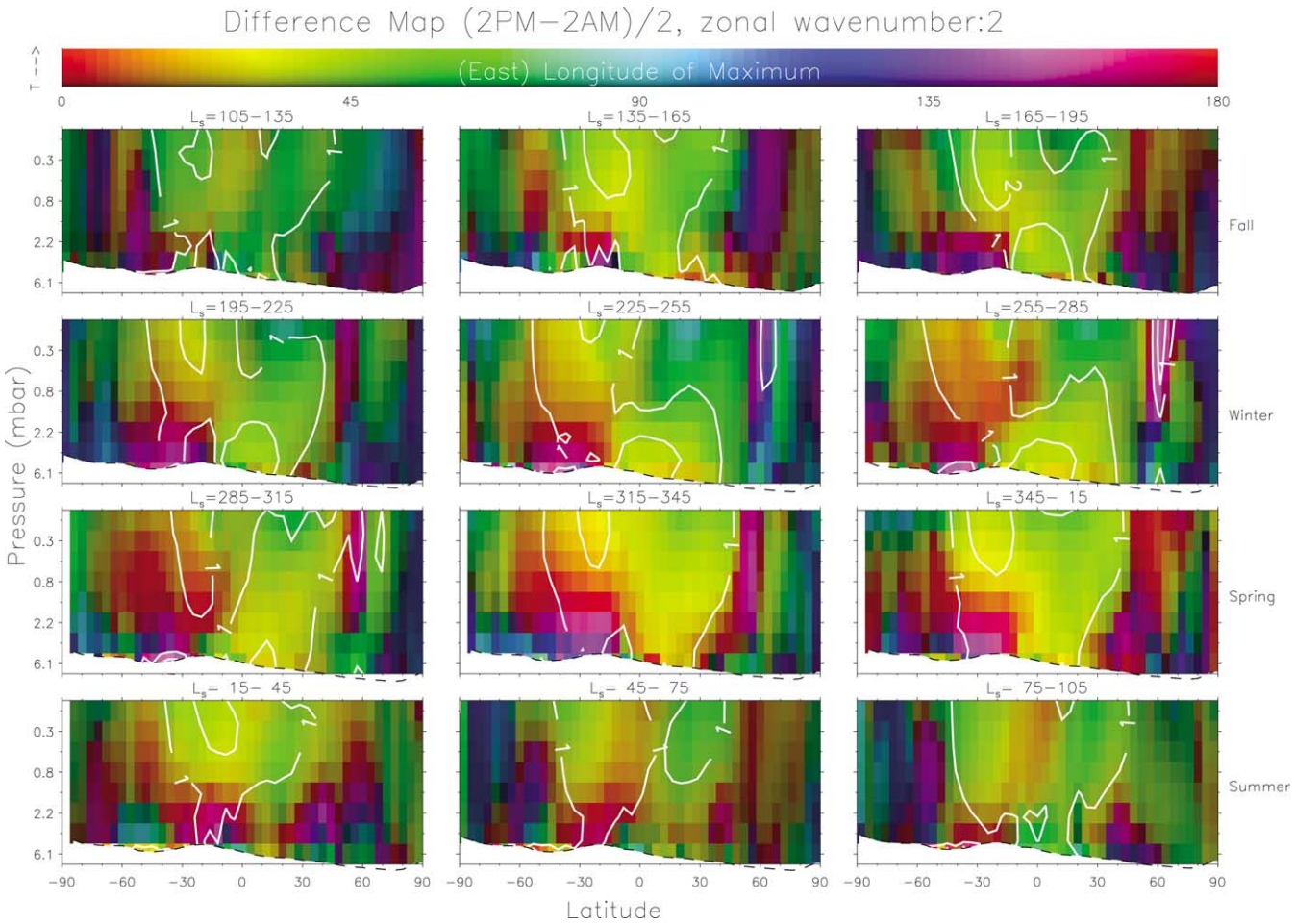

Fig. 11. Same format as Fig. 9, showing the amplitude and phase (East longitude of maximum) of the ($m = 2$) difference maps (2PM–2AM)/2. These maps are dominated by the $\sigma = 1$, $s = -1$ diurnal Kelvin wave (DK1), with contributions from a non-migrating diurnal tide ($\sigma = 1$, $s = 3$).

reflect some power from the other diurnal tide contributing to these maps, or perhaps a higher odd harmonic tide mode.

Wilson and Hamilton (1996) studied the diurnal period, $s = 1$ Kelvin wave in the GFDL MGCM and noted that its amplitude approached that of the migrating diurnal tide for low dust cases. We find an amplitude slightly smaller than they show in their Fig. 17a, about 2 K to their 3 K. They also show the amplitude increasing with height into the winter hemisphere (north for their $L_s \sim 270°$ simulation), which differs notably from our results showing amplitude increasing to the south with height for all seasons. They do note that the behavior of the Kelvin wave with height is quite sensitive to the details of the zonal mean circulation. Also in their Fig. 17d is a representation of the phase of the zonal wind due to the Kelvin wave in their model, and it shows very little phase change across the whole domain. This is very consistent with our results, where their regions with appreciable Kelvin wave amplitude differ in phase by less than 60 degrees of longitude.

The $s = 2$ observations of Hinson et al. (2001) also contain the diurnal Kelvin wave (DK1), and they claim it dominates their observations above about 2 mbar. Our results for $L_s \sim 75°$–$105°$ and 66°N (where their observations are located) are similar to theirs for altitudes above 2 mbar. We find amplitudes of slightly less than 1 K; they find them of order 1 K. We show a maximum near 45°E, as do they. Similar to the good accord between our results found for the $s = 1$ stationary wave, this suggests that the diurnal Kelvin wave during northern summer is relatively reproducible from one martian year to the next.

4.8. Average maps, $m = 3$

These maps (not shown) are dominated by the $s = 3$ stationary wave ($\sigma = 0$), but also have contributions from nonmigrating tides ($\sigma = 2$, $s = -1$ and $\sigma = 2$, $s = 5$). As with the $m = 2$ average map, we expect the nonmigrating westward propagating thermal tides to have negligible amplitude, compared to the stationary waves based on experience with GCM results. We do not show these maps, because their amplitude is significantly smaller than all of the other displayed maps for all seasons throughout our domain. In all seasonal segments, the maximum is of order 2–4 K, and is always located in the lowest scale height of the

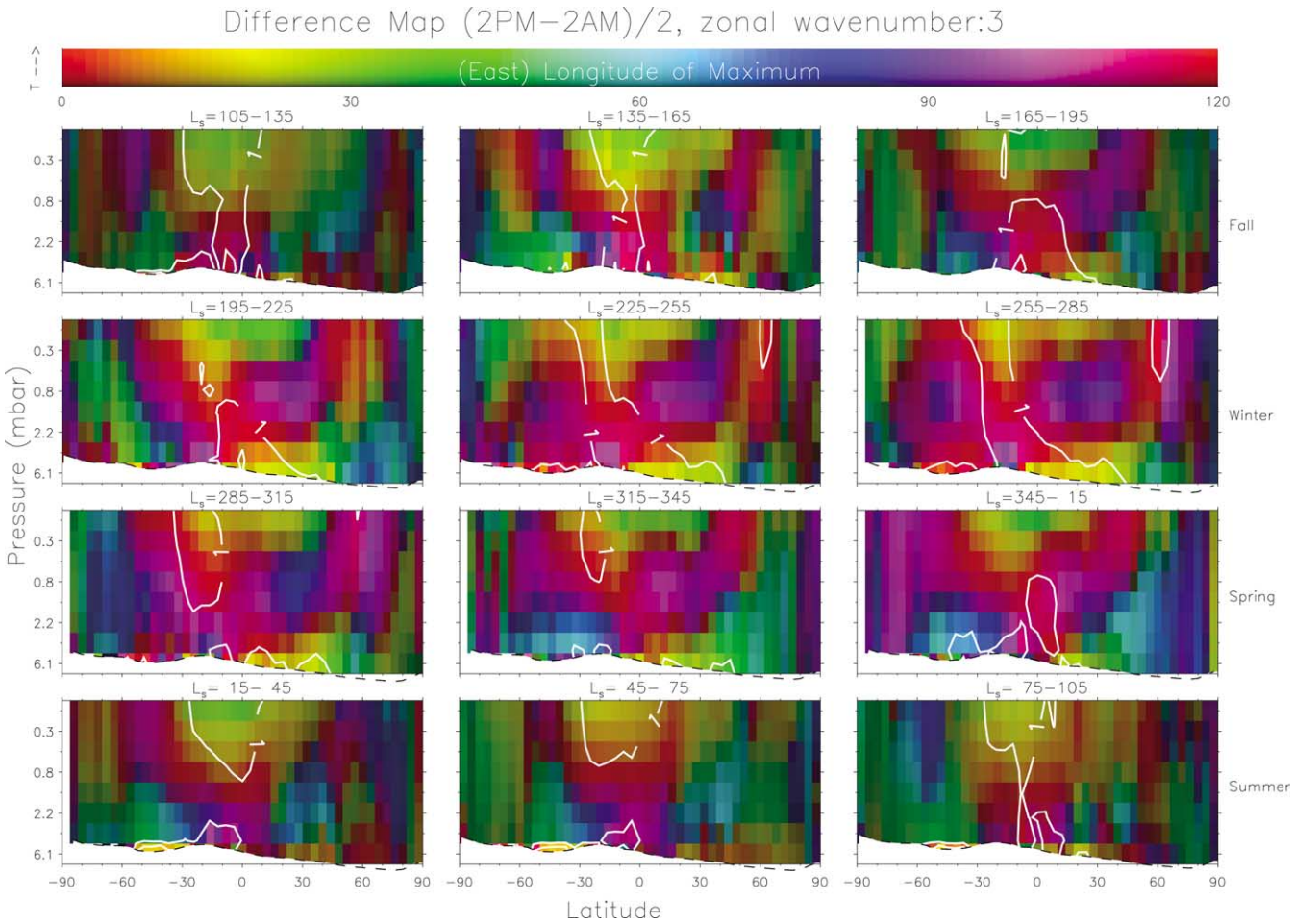

Fig. 12. Same format as Fig. 9, showing the amplitude and phase (East longitude of maximum) of the ($m = 3$) difference maps (2PM–2AM)/2. These maps are dominated by the $\sigma = 1$, $s = -2$ diurnal Kelvin wave with contributions from a nonmigrating tide ($\sigma = 1$, $s = 4$).

atmosphere, in the subtropics and tropics, more often near 45°S. More typical amplitudes are of order 0–1 K in the rest of our domain. The maximum near the surface being located near 45°S is consistent with the topographic forcing, which also has a maximum for $m = 3$ at about 45°S. Only in $L_s \sim$ 255°–285° do we see significant $s = 3$ stationary wave amplitude (1.5 K) propagating to altitudes above 2.2 mbar, then over 60°N latitude, in the winter polar jet. Typically, the amplitude has fallen off to less than 1 K at pressures less than 2.2 mbar, even in the winter polar ducts that propagate the longer stationary waves to high altitudes. Generally, it appears that the $s = 3$ stationary wave cannot effectively propagate vertically like the longer stationary waves, which is consistent with our calculations of the index of refraction of this wave mode.

This inability to propagate for the $s = 3$ stationary wave was also noted in Hollingsworth and Barnes (1996) and Barnes et al. (1996), although both of those modeling efforts showed somewhat greater vertical propagation than we have observed. Both works report a phase of maximum for the northern winter $s = 3$ stationary wave of about 110°E. Our results for $L_s \sim$ 255°–285° suggest an amplitude of maximum of about 45°E, in disagreement with the modeling efforts. It is quite possible that rather than the $s = 3$ stationary wave, the northern winter polar jet region is being dominated instead by one of the nonmigrating tide modes that alias into these maps, explaining the poor comparison. We do not believe that the results of this map are noise as the phase structure (while different than modeling) is quite repeatable throughout the year, and relatively smooth as a function of latitude. We would expect noise to be essentially uncorrelated between latitudes as the noise between those observations is completely independent. Furthermore, typical amplitudes are of order 0.5 K, and this is above our estimates of amplitude uncertainty.

4.9. Difference maps, m = 3

The $m = 3$ difference maps (Fig. 12) are likely dominated by the nonmigrating tide $\sigma = 1$, $s = -2$ (dominated by the $s = -2$ diurnal Kelvin wave, DK2) but also contributing is the nonmigrating tide with $\sigma = 1$, $s = 4$. As with the $m = 2$ difference maps, the expected amplitudes and vertical wavelength differences between the diurnal Kelvin wave

and the nonmigrating westward propagating thermal tide, coupled with the vertical smoothing of our observations effectively selects only the diurnal Kelvin wave for these maps. Wilson (2000) also identified the diurnal Kelvin wave DK2 in a subset of TES data processed to mimic the IRTM T15 weighting function (25 km altitude temperature). He points out that the T15 analysis is more sensitive to the diurnal Kelvin waves than the westward nonmigrating tides because of their vertical wavelengths. Wilson reports that the diurnal Kelvin wave DK2 has a vertical wavelength of about 90 km, while the other tide mode contributing here has a vertical wavelength of less than 33 km. We are likely experiencing the same filtering based on vertical wavelength in this analysis. As mentioned in the limitations of our data set, the vertical wavelengths resolved are limited by the contribution functions for the instrument's bandpasses which are roughly 1–2 scale heights (10–20 km). Therefore, we too are relatively insensitive to the short vertical wavelength $\sigma = 1$, $s = 4$ nonmigrating tide, but fully sensitive to the long vertical wavelength $\sigma = 1$, $s = -2$ diurnal Kelvin wave, DK2.

Consistent with Wilson (2000), the amplitude and phase structure of these maps are nearly constant throughout the year. Amplitudes exceed 1 K in the tropics (slightly stronger in the south), and appear to grow slowly with altitude. Phase is roughly consistent (considering the amplitude and phase changes with height) with that shown in Wilson (2000). We find a maximum near longitude 0° for altitude 25 km, and phase advancing eastward with height with a vertical wavelength of about 60 km. This wavelength is slightly shorter than Wilson suggests for the DK2, but perhaps we are still seeing some influence from the shorter vertical wavelength westward nonmigrating tide mode, confusing the interpretation. As mentioned in Wilson (2000), it is likely that the DK2 mode grows with height above the domain of our analysis to become a significant perturbation at aerobraking altitudes. Indeed this is demonstrated in Wilson (2002), where aerobraking data support the idea that DK2 (and DK1) extends to 130 km and significantly shapes the observed density structure there. Hence, the 1 K signal we report here for the lower atmosphere is significant to upper atmospheric studies.

5. Meridional heat transports

Figs. 13 and 14 show composite profiles of the zonal mean temperature and the $s = 1$, 2, and 3 stationary wave modes as a function of longitude and height for latitudes 60°N and 60°S respectively. These figures show the relative strength of expression in the temperature structure of the lapse rate versus the $s = 1$ and $s = 2$ stationary waves. In the spring and summer hemispheres, the lapse rate dominates the temperature structure, but slight stationary wave perturbations are still evident. In the fall and winter hemispheres, the lapse rates invert, with temperature increasing upward. While the lapse rates are inverting, the stationary waves dominate the temperature structure in these plots. One aspect of the stationary waves that can easily be addressed from these maps and those of amplitude and phase shown above are the meridional heat transports carried in the stationary waves. Westward phase tilts with height in the stationary waves are indicative of poleward heat transport. Examining the 60°N composite plots, it is evident that the stationary wave perturbations are barotropic, with no significant longitudinal tilts with height in the maxima. However, the 60°S composite plots during southern fall and winter show moderate westward tilt with height of the temperature maxima.

Comparing our results with the models from Hollingsworth and Barnes (1996) we find that they accurately predicted negligible phase tilts with height in the northern winter for $s = 2$ stationary waves. However, for $s = 1$ stationary waves in northern winter, they predicted a phase tilt with height of about 60° longitude over 4 scale heights, much greater than the negligible tilt we observed for this wave at this time. Barnes et al. (1996) only showed a slight phase change with height of both the $s = 1$ and $s = 2$ stationary waves at northern winter solstice.

In the southern winter, Hollingsworth and Barnes's (1996) results showed a negligible phase tilt with height for the $s = 2$ stationary wave, consistent with our findings. However, for the $s = 1$ stationary wave at the same time, they found a smaller phase tilt with height than is found in our results. They found a phase tilt of about 60° of longitude over 4 scale heights versus about 120° of longitude over 4 scale heights in our results. Its unclear how much of this discrepancy is due to the assumptions of their model, or the inaccuracies of their topographic forcing (Mars Consortium topography estimates). Barnes et al. (1996) (also using Mars Consortium topography estimates) found a more comparable phase tilt with height for the $s = 1$ stationary wave in southern winter, roughly 100° of longitude over 4 scale heights (estimated from their Fig. 8). Both of these results are somewhat less than what we found, suggesting that their results underestimated the contribution of the $s = 1$ stationary wave to meridional heat transport in the southern winter. Barnes et al. (1996) note that the $s = 1$ stationary wave poleward heat transport they found is the dominant component of eddy poleward heat transport in the south, but not in the north (where transient waves dominate their eddy poleward heat transport). Our findings of similar $s = 1$ stationary wave poleward heat transport at northern winter solstice and greater $s = 1$ stationary wave poleward heat transport in the southern winter support and strengthen the conclusions of Barnes et al. (1996), that stationary wave poleward heat transport is the dominant component of eddy poleward heat transport for the southern winter, but is insignificant for the northern winter. Of course, these conclusions will need to be reexamined after the analysis of transient waves from the TES data.

We have computed the magnitudes of the meridional heat transports due to the stationary waves assuming ther-

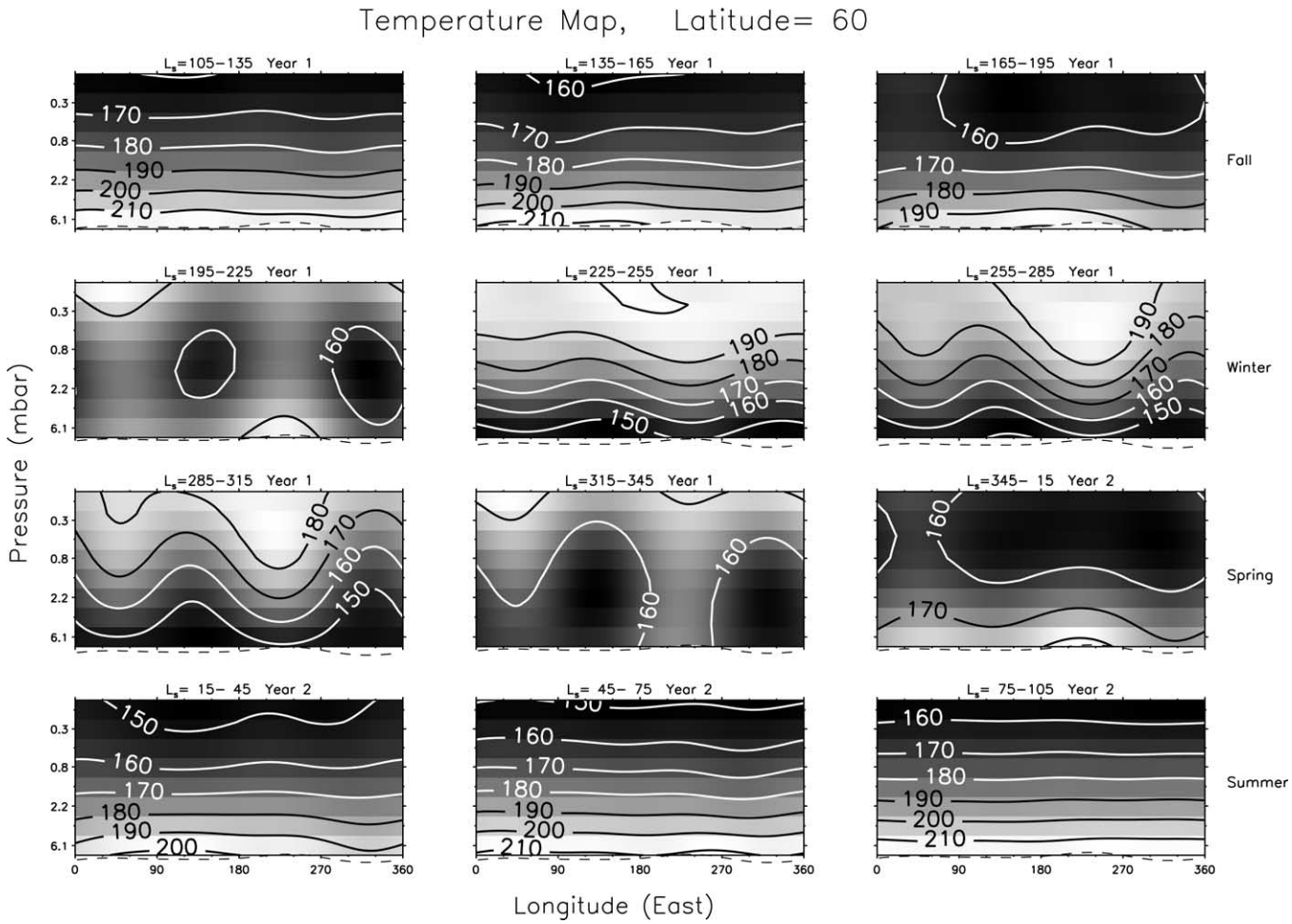

Fig. 13. Seasonal variation of composites of zonal mean temperature and $s = 1, 2, 3$ stationary waves as a function of longitude and height for 60°N. Each panel represents 30° of L_s as on the previous plots, but the abscissa represents longitude at 60°N. Temperature is indicated by both the grayscale (bright is hot) and contours, labeled in kelvin. An estimate of the topographically varying surface pressure ($m = 0, 1, 2, 3$) is indicated by the blanked region and the dashed line at or below the bottom of the plot. Note the reversal of the lapse rate, and the barotropic nature of the stationary waves. Note also that the stationary wave temperature maxima are generally in phase with high topography during northern fall and winter ($L_s \sim 195°$–$15°$). $s = 1$ tends to dominate the other stationary waves near the top of the domain, while $s = 2$ dominates closer to the surface.

mal wind balance and that eddy meridional velocities are zero ($v' = 0$) at the surface. The amplitude and phase plots (Figs. 9 and 10) suggested that the most significant contributor to meridional heat flux from the stationary waves is the $s = 1$ stationary wave during southern winter. Fig. 15 shows this, confirming our estimates, with heat fluxes reaching as large as -40 K m/s in the southern winter polar vortex, while those in the northern winter polar vortex are no larger than $+12$ K m/s. In the south, the meridional heat flux is larger than -10 K m/s from $L_s \sim 345°$ until $L_s \sim 195°$, more than half of the year. This maximum in heat flux is found in the polar jet itself, at the top of our domain (although the density-weighted heat flux peaks at about 2 scale heights above the surface). Interestingly, from $L_s \sim 195°$–$225°$, the $s = 1$ stationary wave carries heat *equatorward* in the southern hemisphere on the poleward edge of the polar jet, with an amplitude almost as large as the maximum fluxes in the north, $+5$ K m/s. In the northern winter, the $s = 1$ stationary wave only carries appreciable heat meridionally from $L_s \sim 195°$ until $L_s \sim 315°$. Even then, the typical amplitudes are only $+5$ K m/s, less than 1/3 the typical magnitudes seen during southern winter. Barnes et al. (1996) also plot the stationary eddy meridional heat fluxes (their Figs. 5a and 11) from their model. They find meridional fluxes of about $+10$ K m/s in the northern winter, which is roughly consistent with our computed heat flux in the north.

We do not show the meridional heat flux from the $s = 2$ stationary wave as it is significantly smaller than the $s = 1$ stationary wave. Even comparing only the northern winter heat fluxes, the $s = 2$ stationary wave contribution is reduced by a factor of about 2 from the $s = 1$ stationary wave contribution, with peak fluxes of about $+7$ K m/s. In the south, as with the $s = 1$ stationary wave, the amplitudes are slightly larger, but only reach as large as about -13 K m/s near the top of the polar jet. Generally, the contributions of the $s = 2$ stationary wave to meridional heat flux are small relative to the $s = 1$ stationary wave.

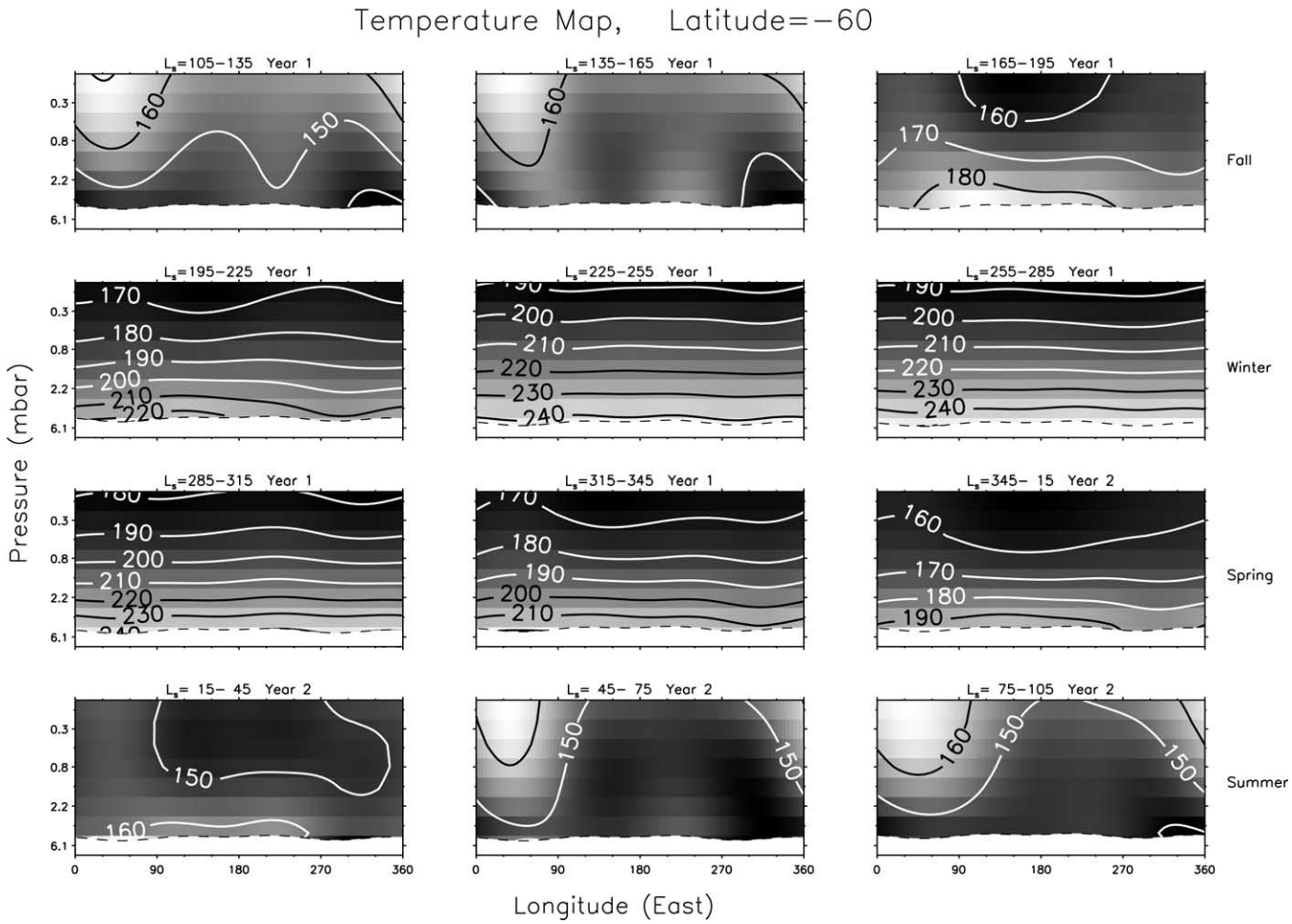

Fig. 14. Same format as Fig. 13, but for 60°S. In this case, note the westward phase tilt with height of the stationary waves during southern fall and winter ($L_s \sim 15°$–$195°$). Note also that generally $s = 1$ dominates the other stationary waves in these plots especially when the amplitudes are larger.

It is also interesting to examine the heating rate due to the stationary waves, expressed in terms of a rate of change of temperature. This is proportional to the convergence of the meridional heat fluxes discussed above, and is shown in Fig. 16. This figure highlights that the stationary waves are much more important to the atmospheric energy budget in southern winter than in northern winter. In the peak of southern winter ($L_s \sim 75°$–$105°$), the $s = 1$ stationary wave causes a cooling as large as -3 K/Sol at the top of our domain above 45°S (on the equatorward edge of the polar jet), and a heating of as large as $+6$ K/Sol at the top of our domain above 65°S (on the poleward edge of the polar jet). In the northern winter, the heating rates never exceed $+2$ K/Sol in our domain, but again the maxima (of opposite sign) straddle the polar jet and are at the top of our domain. Typically, the heating rate due to the $s = 1$ stationary wave dominates over the other zonal wavenumbers, but occasionally the $s = 2$ stationary wave contribution approaches within a factor of two of that of the $s = 1$ stationary wave.

We can directly compare these heating rates with the published values in Haberle et al. (1993) (their Fig. 31a). They report stationary wave heating rates for a model simulation of northern winter with low dustiness. Their results suggest a cooling as large as -3.5 K/Sol, 2.5 scale heights above 50°N, and a heating larger than $+1$ K/Sol, 4 scale heights above 70°N. This roughly agrees with our results for that season, which show a cooling of about -1 K/Sol slightly higher in the atmosphere than they found above 50°N, and a heating of about $+2$ K/Sol nearly coincident with their maximum heating. Haberle et al. (1993) also show the heating rates due to transient wave heating ($\pm\sim 5$ K/Sol straddling the polar jet), and the mean meridional circulation (more than $+10$ K/Sol at 40°N and about -10 K/Sol at about 70°N). Their results suggest that stationary wave heating ranks at the bottom of the list of dynamical heating sources for northern winter. To assess the heat transports due to the meridional circulation using the TES data is a very difficult task, but the transient waves can be analyzed much like the stationary waves here. Whether the relative strengths of the stationary wave and transient wave heat transports predicted by Haberle et al. (1993) agree with the TES data will have to wait for a similar analysis of the transient waves.

Our results suggest that the stationary waves are much

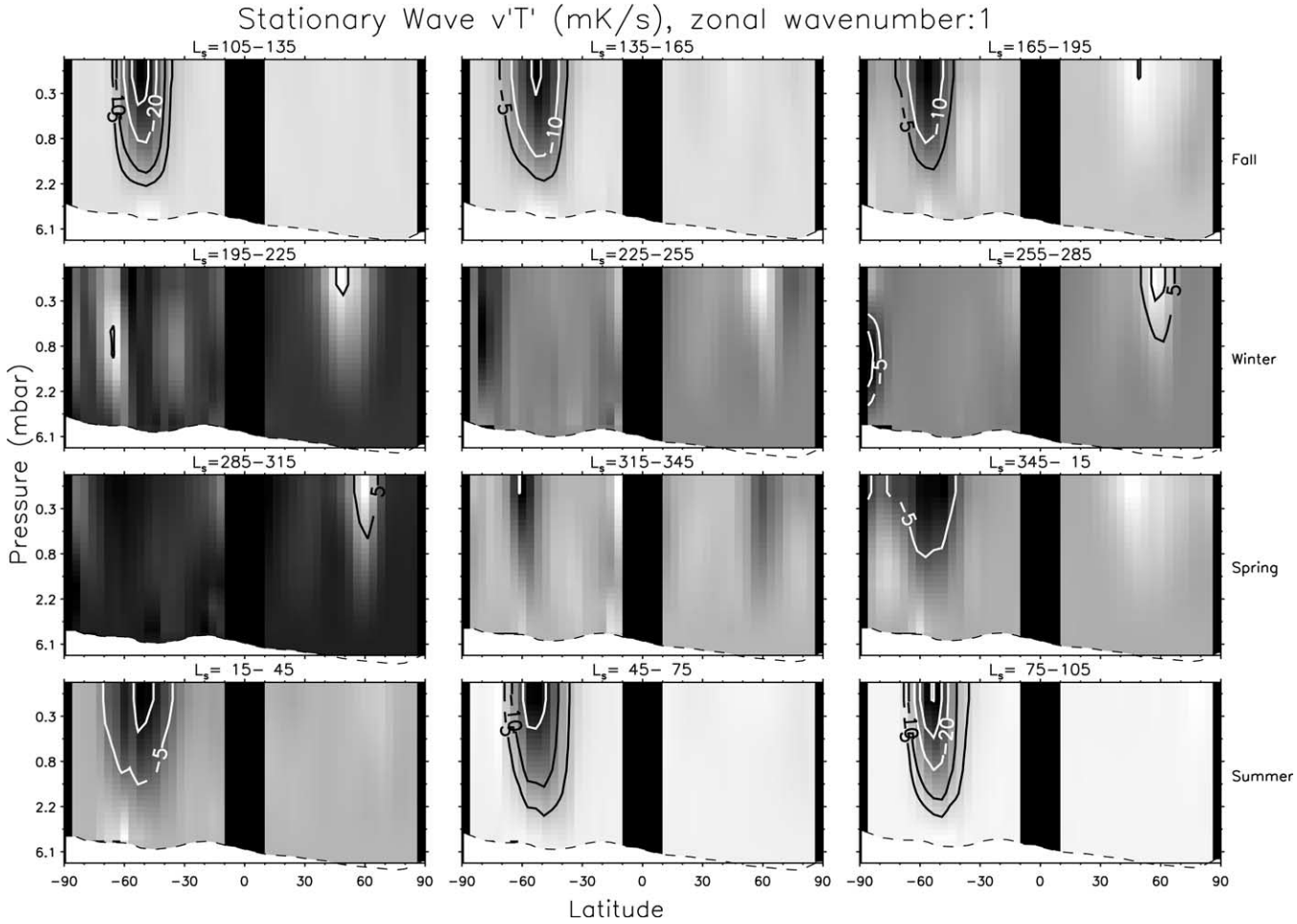

Fig. 15. Same format as Fig. 2, showing the amplitude of the meridional heat flux, $v'T'$, in units of K m/s from the $s = 1$ stationary wave. In addition to the labeled contours, dark regions represent high southward heat fluxes, and bright regions represent high northward heat fluxes. Westward phase tilts in the stationary wave imply poleward heat fluxes. On Mars, the southern winter stationary wave carries a significant amount of heat poleward in the polar jet, about 4 times that of the northern winter stationary wave.

more important in the southern winter. For that time of year, Pollack et al. (1990) have published model calculations of the relative magnitudes of various atmospheric heating sources. Their Fig. 6a and 6c suggests that stationary waves carry about 2×10^{13} W poleward in late southern spring and late southern winter, dominating over the heat transport due to transient waves. This is similar to the magnitude of the vertically integrated stationary wave heat flux we observe in the southern hemisphere late spring and winter. However, differing from our results, their modeled stationary wave heat flux reverses (equatorward) for the peak of southern winter, yet maintains roughly the same magnitude. We see no evidence of this flux reversal in our results with the strongest poleward fluxes coming at the peak of southern winter. Judging from Pollack et al.'s (1990) results, we expect that the stationary wave heating around the southern winter polar jet to dominate over transient wave heating, and it may be as large as 25% of the condensation flow heat flux which mainly balances the polar night atmospheric radiation to space. Thus, while the stationary wave heat flux is rarely the dominant contributor to the overall atmospheric heating, it is frequently significant, particularly in the southern winter.

6. Summary

We have analyzed the temperature retrievals from TES nadir spectra to yield latitude–height-resolved maps of various atmospheric wave modes as a function of season for a full Mars year. We were able to isolate specific modes by averaging or differencing the two sets of observations at different local times and then Fourier analyzing the results in longitude. Among the isolated wave modes is the zonal mean, time mean temperature, which we then used to derive zonal mean zonal winds and quasi-geostrophic indices of refraction for the longest stationary waves. We also isolated a limited representation of the migrating diurnal tide, although with observations at only two local times, it is impossible to constrain both the amplitude and phase of this

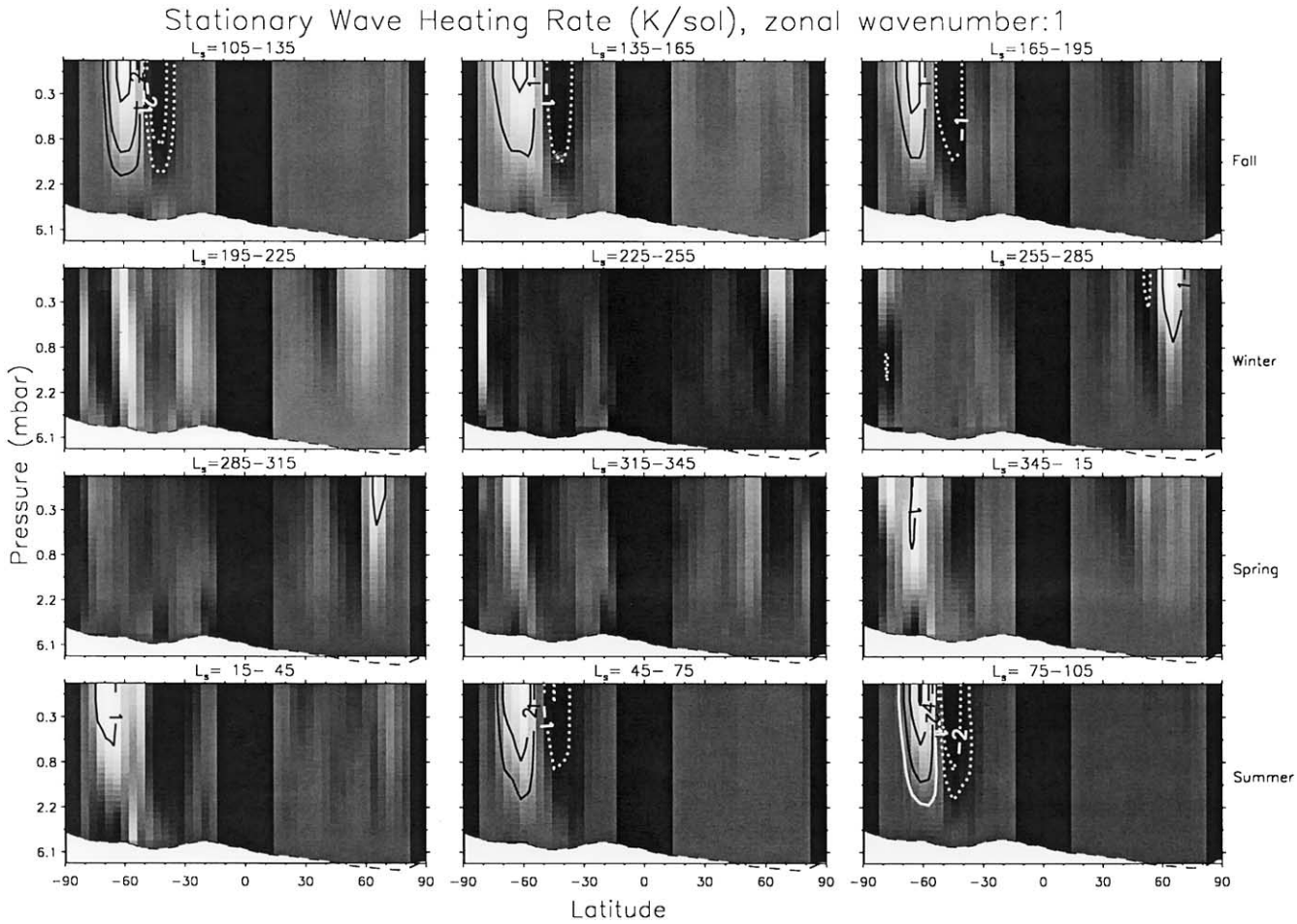

Fig. 16. Same format as Fig. 2, showing the heating rate in units of K/Sol from the $s = 1$ stationary wave. This is proportional to the convergence of the meridional heat flux shown in Fig. 15. Contour intervals are 1 K/Sol, with the zero contour removed, and negative contours are dotted. Dark regions represent cooling and bright regions represent heating. Typical heating rates in the southern winter polar jet are about 2 K/Sol or more, while in the north, they rarely reach 1 K/Sol.

mode. GFDL MGCM results were used to aid in scientifically interpreting the tidal measurements. The diurnal Kelvin wave (DK1) was isolated in the data, with results roughly consistent with models (Wilson and Hamilton, 1996) The $s = 2$ diurnal Kelvin wave (DK2) was also isolated in the data, consistent with the work of Wilson (2000). Both of these modes may represent a significant perturbation after their propagation to aerobraking altitudes.

The $s = 1$, 2, and 3 stationary wave modes were also isolated and mapped. The $s = 1$ and $s = 2$ stationary waves were found to have significant amplitude in ducts extending up the winter polar jets, while the $s = 3$ was found to be confined to near the surface. The indices of refraction echoed the existence of deep winter polar jet ducts for the long wavelength stationary waves, disappearing quickly for $s = 3$ or higher. The $s = 1$ stationary wave was found to have little phase tilt with height during northern winter, but significant westward phase tilt with height in the southern winter. This indicates that the wave carries heat poleward, (of order 20 K m/s) and in comparison to the results of Barnes et al. (1996), the observations carry slightly more than the model predictions for southern winter. Finally, we noted that the phase of the $s = 2$ stationary wave was nearly constant with time, but the $s = 1$ wave migrated east by about 90° of longitude from fall to winter and back again to spring in the North. This is consistent with the $s = 1$ wave being near resonance during northern winter solstice.

MGS and TES continue to take data, extending the record beyond the single Mars year of this analysis. Future work will be able to assess the interannual variability of these observations, and how dust opacity differences effect the forced waves. Overall, these results provide the first comprehensive benchmark for forced waves in Mars' atmosphere against which future atmospheric models of Mars can be compared.

References

Andrews, D.G., Holton, J.R., Leovy, C.B., 1987. Middle Atmospheric Dynamics. Academic Press, San Diego.

Banfield, D., Toigo, A.D., Ingersoll, A.P., Paige, D.A., 1996. Martian weather correlation length scales. Icarus 119, 130–143.

Banfield, D., Conrath, B., Pearl, J.C., Smith, M.D., Christensen, P., 2000. Thermal tides and stationary waves on Mars as revealed by Mars Global Surveyor thermal emission spectrometer. J. Geophys. Res. 105, 9521–9537.

Barnes, J.R., Haberle, R.M., Pollack, J.B., Lee, H., Schaeffer, J., 1996. Mars atmospheric dynamics as simulated by the NASA Ames general circulation model. 3. Winter quasi-stationary eddies. J. Geophys. Res. 101, 12753–12776.

Bridger, A.F.C., Murphy, J.R., 1998. Mars' surface pressure tides and their behavior during global dust storms. J. Geophys. Res. 103, 8587–8601.

Chapman, S., Lindzen, R.S., 1970. Atmospheric Tides. Reidel, Dondrecht.

Christensen, P.R., Anderson, D.L., Chase, S.C., Clark, R.N., Kieffer, H.H., Malin, M.C., Pearl, J.C., Carpenter, J., Bandeira, N., Brown, F.G., Silverman, S., 1992. Thermal emission spectrometer experiment—Mars-Observer mission. J. Geophys. Res. 97, 7719–7734.

Christensen, P.R. and 25 Co-Authors, 2001. The Mars Global Surveyor Thermal Emission Spectrometer experiment: investigation description and surface science results. J. Geophys. Res. 106, 23823–23871.

Conrath, B.J., 1976. Influence of planetary-scale topography on the diurnal thermal tide during the 1971 martian dust storm. J. Atmos. Sci. 33, 2430–2439 .

Conrath, B.J., 1981. Planetary-scale wave structure in the martian atmosphere. Icarus 48, 246–255.

Conrath, B.J., Pearl, J.C., Smith, M.D., Maguire, W.C., Christensen, P.R., Dason, S., Kaelberer, M.S, 2000. Mars Global Surveyor Thermal Emission Spectrometer (TES) observations: atmospheric temperatures during aerobraking and science phasing. J. Geophys. Res. 105, 9509–9519.

Forbes, J.M., Hagan, M.E., 2000. Diurnal Kelvin wave in the atmosphere of Mars: towards an understanding of "stationary" density structures observed by the MGS accelerometer. Geophys. Res. Lett. 27, 3563–3566.

Haberle, R.M., Pollack, J.B., Barnes, J.R., Zurek, R.W., Leovy, C.B., Murphy, J.R., Lee, H., Schaeffer, J., 1993. Mars atmospheric dynamics as simulated by the NASA Ames general circulations model. 1. The zonal-mean circulation. J. Geophys. Res. 98, 3093–3123.

Hinson, D.P., Tyler, G.L., Hollingsworth, J.L., Wilson, R.J., 2001. Radio occultation measurements of forced atmospheric waves on Mars. J. Geophys. Res. 106, 1463–1480.

Hollingsworth, J.L., Barnes, J.R., 1996. Forced stationary planetary waves in Mars's winter atmosphere. J. Atmos. Sci. 53, 428–448.

Hollingsworth, J.L., Haberle, R.M., Barnes, J.R., Bridger, A.F.C., Pollack, J.B., Lee, H., Schaeffer, J., 1996. Orographic control of storm zones on Mars. Nature 380, 413–416.

Lindzen, R.S., 1970. The application and applicability of terrestrial atmospheric tidal theory to Venus and Mars. J. Atmos. Sci. 27, 536–549.

Martin, T.Z., Kieffer, H.H., 1979. Thermal infrared properties of the martian atmosphere. 2. 15 μm band measurements. J. Geophys. Res. 84, 2843–2852.

Nayvelt, L., Gierasch, P.J., Cook, K.H., 1997. Modeling and observations of Martian stationary waves. J. Atmos. Sci. 54, 986–1013.

Palmer, T.N., 1982. Properties of the Eliassen–Palm flux for planetary scale motions. J. Atmos. Sci. 39, 992–997.

Pearl, J.C., Smith, M.D., Conrath, B.J., Bandfield, J.L., Christensen, P.R., 2001. Observations of Martian ice clouds by the Mars Global Surveyor Thermal Emission Spectrometer: the first Martian year. J. Geophys. Res. 106, 12325–12338.

Pirraglia, J.A., Conrath, B.J., 1974. Martian tidal pressure and wind fields obtained from Mariner-9 infrared spectroscopy experiment. J. Atmos. Sci. 31, 318–329.

Pollack, J.B., Haberle, R.M., Schaeffer, J., Lee, H., 1990. Simulations of the general circulation of the martian atmosphere. 1. Polar processes. J. Geophys. Res. 95, 1447–1473.

Richardson, M.I., Wilson, R.J., 2002. Investigation of the nature and stability of the martian seasonal water cycle with a general circulation model. J. Geophys. Res. 107, 10.1029/2001JE001536.

Smith, M.D., 2002. The annual cycle of water vapor on Mars as observed by the Thermal Emission Spectrometer. J. Geophys. Res., in press.

Smith, D.E., Zuber, M.T., Solomon, S.C., Phillips, R.J., Head, J.W., Garvin, J.B., Banerdt, W.B., Muhleman, D.O., Pettengill, G.H., Neumann, G.A., Lemoine, F.G., Abshire, J.B., Aharonson, O., Brown, C.D., Hauck, S.A., Ivanov, A.B., McGovern, P.J., Zwally, H.J., Duxbury, T.C., 1999. The global topography of Mars and implications for surface evolution. Science 284, 1495–1503.

Smith, M.D., Pearl, J.C., Conrath, B.J., Christensen, P.R., 2000. Mars Global Surveyor Thermal Emission Spectrometer (TES) observations of dust opacity during aerobraking and science phasing. J. Geophys. Res. 105, 9539–9552.

Smith, M.D., Pearl, J.C., Conrath, B.J., Christensen, P.R., 2001. Thermal Emission Spectrometer results: Mars atmospheric thermal structure and aerosol distribution. J. Geophys. Res. 106, 23929–23945.

Smith, M.D., Conrath, B.J., Pearl, J.C., Christensen, P.R., 2002. Thermal Emission spectrometer observations of martian planet-encircling dust storm 2001A. Icarus 157, 259–263.

Wilson, R.J., 2000. Evidence for diurnal period Kblvin waves in the martian atmosphere from Mars Global Surveyor TES data. Geophys. Res. Lett. 27, 3889–3892.

Wilson, R.J., 2002. Evidence for nonmigrating thermal tides in the Mars upper atmosphere from the Mars Global Surveyor accelerometer experiment. Geophys. Res. Lett. 29, 10.1029/2001GL013975.

Wilson, R.J., Hamilton, K., 1996. Comprehensive model simulation of thermal tides in the martian atmosphere. J. Atmos. Sci. 53, 1290–1326.

Wilson, R.J., Richardson, M.I., 2000. The martian atmosphere during the Viking mission. I. Infrared measurements of atmospheric temperatures revisited. Icarus 145, 555–579.

Zurek, R.W., 1976. Diurnal tide in the martian atmosphere. J. Atmos. Sci. 33, 321–337.